Synthesis, Cation Distribution, and Disorder of Fast-Ion Conducting Pyrochlore Oxides : A Combined Neutron and X-Ray Rietveld Analysis

By

Esther M. Ku

B.A. Chemistry

Columbia College, Columbia University, 1995

Submitted to the Department of Materials Science and Engineering in Partial Fulfillment of the Requirements for the Degree of

MASTER OF SCIENCE IN MATERIALS SCIENCE AND ENGINEERING

at the

Massachusetts Institute of Technology

February 1999

Signature of Author: _____

Department of Materials Science and Engineering
January 15, 1999

Certified by: _____

Bernhardt J. Wuensch
Professor of Ceramics

Accepted by: _____

Linn W. Hobbs
John F. Elliott Professor of Materials
Chairman, Departmental Committee on Graduate Students

Synthesis, Cation Distribution, and Disorder of Fast-Ion Conducting Pyrochlore Oxides : A Combined Neutron and X-Ray Rietveld Analysis

By

Esther M. Ku

Submitted to the Department of Materials Science and Engineering on
January 15, 1999
in Partial Fulfillment of the Requirements for the Degree of
MASTER OF SCIENCE IN MATERIALS SCIENCE AND ENGINEERING

Abstract

Fast-ion conducting pyrochlore oxides, multi-metal compounds with the general formula $A_2B_2O_7$, are subject to growing interest because of their potential use as fuel cell materials. This study focuses on a specific fast-ion conducting solid solution series, $Y_2(Zr_ySn_{1-y})_2O_7$. Polycrystalline $Y_2(Zr_ySn_{1-y})_2O_7$ powders, where y=0.2, 0.4, 0.6 and 0.8, were synthesized using a newly-devised variation of the Pechini method. Details on the specific metal precursors, technique, heating schedules, as well as an extensive examination of literature have been developed to provide useful guidelines in the preparation of mixed-cation oxide powders via the liquid-mix approach. Through the use of combined neutron and x-ray diffraction data, a Rietveld structural analyses were conducted to explore the disordering behavior and cation distribution. This particular solid solution series was chosen with the hope of reconciling differences in the behavior of $Y_2(Zr_yTi_{1-y})_2O_7$, a system displaying increased disorder in the anion and cation arrays with increasing y, and $Y_2(Sn_yTi_{1-y})_2O_7$, an essentially ordered system. Results from the structural analyses of the $Y_2(Zr_ySn_{1-y})_2O_7$ series show marked similarities with the previously-studied $Y_2(Zr_yTi_{1-y})_2O_7$. Like the Ti zirconates, the O(1) coordinate x decreased quadratically as opposed to the linear decrease in the Ti stannates. Oxygen disorder in the Sn zirconates begin almost immediately upon substitution of Zr^{4+} in solid solution, and is complete slightly beyond y=0.8, resulting in a defect fluorite phase .

The cation partitioning of the three cations, Sn^{4+}, Zr^{4+}, and Y^{3+}, in the two cystallographically independent sites, A and B, cannot be determined from a single diffraction experiment. Determination of the cation distribution had consequently never been determined for a pyrochlore oxide. Therefore, through the use of linear constraints and the methodical refinement technique previously developed, x-ray and neutron diffraction data were both used in the present work in an attempt to determine the cation distribution in the pyrochlore structure. As was found in the Ti-zirconates, a fluorite-like phase possessing a slightly larger lattice parameter co-existed with the pyrochlore solid solutions. This, in conjunction with the weakening of superstructure intensities with increasing Zr content in the series led to increased

residuals and larger standard deviations in the refined parameters as the structure disordered. The results reveal that a small, fixed amount of Sn occupies the A site in substitution for Y^{3+} in the low-Zr, well-ordered portion of the solid solution series which is consistent with the small amount of cation disorder in $Y_2Sn_2O_7$ previously found in studies by Eberman. Furthermore, Zr^{4+} readily enters the A site beginning as early as y=0.2 . The cation partitioning of the Zr^{4+} and Y^{3+} for y=0.4 could not be determined with because the neutron data at this composition shows very little contrast in scattering between the A and B sites. Another independent diffraction experiment can solve this two-cation, one-site problem, but it is likely that nearly equal amounts of the two cations are distributed between the two sites. Overall, the disorder and cation distributions found in this study confirm zirconium's ability to enter the eight-coordinated A site more readily than covalently-bonded Sn. The fact that the progress of cation and anion disorder with increasing Zr content has been shown to be quite similar to that in the $Y_2(Zr_yTi_{1-y})_2O_7$ system, previously show to be an excellent fast-ion conductor, allows one to predict that the newly-synthesized $Y_2(Zr_ySn_{1-y})_2O_7$ compositions will prove to be equally-outstanding conductors.

Thesis Supervisor: Bernhardt J. Wuensch

Title: Professor of Ceramics

Acknowledgements

"From the Causes of things to know the Highest Cause"

Robert Boyle, Chemist

About a year ago I first learned of the motto of the great 17th century chemist, Robert Boyle. I was profoundly inspired by Boyle's life and his open, honest, and humble approach toward scientific discovery and thinking. His motto succinctly articulates my deep gratitude toward the Creator for the opportunity to learn more about the "Causes of things" in materials science. Jesus Christ has not only been my God, but also my personal tutor and coach when I lacked both the knowledge and understanding to complete this thesis. To Him I dedicate this work.

I would also like to thank both my natural and spiritual families who have been a tremendous support and comfort to me at times when I needed it the most. Their prayers and encouragement have helped see me through graduate school.

Bernie Wuensch, my adviser, has astounded me at times with his creative curiosities, artistic teaching-style, delightful humor, and patience. I could not have been more fortunate than to have had the opportunity to learn under his tutelage.

Many key players in the Department of Materials Science offered practical suggestions and help on the thesis. Kevin Eberman first introduced me to the mysteries of the Pechini method, pyrochlores, and Rietveld analyses. He gave me the idea of conducting an extensive literature review on the Pechini method and devoted much of his time and energies in answering my basic questions. Evy Yeo helped to clear a path for me in her preliminary studies of the same solid solution series. Hitoshi Takamura from the Tuller group was critical in helping me use the Rietan program. He spent hours helping me to get the program running, debugging my input files, and providing friendly support this past semester. He was an invaluable resource. I am grateful to other members of the Tuller group including Jason Sprague, Carlos Navas, and Marlene Spears for their useful discussions. I also appreciate the expertise of Timothy McClure from the Center of Materials Science and Engineering, who collected the thermogravimetric data; Joseph Adario and Peter Kloumann in the use of the Rigaku x-ray diffractometer; and Fred Wilson in everything in-between.

Many thanks to Dr. Judith Stalick at the National Institute of Technology, in Gaithersburg, Maryland for collection of the neutron diffraction data. Her willingness to answer my questions and her tutorial on the GSAS and Refine programs came at a critical time to lead me to a deeper understanding of Rietveld refinements.

The number 3.091 has taken on greater significance for me since I began my journey at MIT. My first semester as a teaching assistant, as well as this past semester, quickly instilled in me a greater appreciation for the art of teaching and communication. Sincere thanks to Professor Sadoway, the staff, and students for making it a tremendous learning experience (and a little fun at the same time). I would also like to acknowledge the U.S. Department of Energy and the Technical Leadership Development Program, which have given me the time wonderful opportunity of returning to school.

Last but not least, I thank all my friends whom I have been blessed to meet here in Cambridge. Their empathy has brought much cheer to my soul, and I have certainly been surrounded by those who have been great listeners and encouragers throughout my brief stay here.

Table of Contents

Abstract 2

Acknowledgements 4

Table of Contents 5

List of Figures 6

List of Tables 7

1: Introduction

1.1 Purpose of this Research 8

1.2 The Pyrochlore Structure 10

1.3 Complementary Use of Neutron and X-Ray Powder Diffraction 14

2: Synthesis of Pyrochlore Oxide Powders 21

2.1 Introduction 21

2.2 Survey of Ceramic Synthesis Utilizing the Pechini Method or Other Polymeric Precursor Techniques 22

2.3 Experimental Synthesis of $Y_2(Zr_ySn_{1-y})_2O_7$ powders via Polymeric Precursors 29

2.3.1 Preparation of Stock Solutions 29

2.3.1.1 Yttrium Citrate 32

2.3.1.2 Tin Citrate 33

A. Aqueous based approach 33

B. Alkoxide precursor approach 34

2.3.1.3 Zirconium Citrate 34

A. Aqueous based approach 34

B. Alkoxide precursor 35

2.3.2 Stock Solution Assay 35

2.3.3 Mixing Stock Solutions for Multi-Metal Compositions 36

2.3.4 Thermogravimetric Analysis (TGA/DTA) 36

2.3.5 Preparation and Processing of Metal Citrate Solutions for $Y_2(Zr_ySn_{1-y})_2O_7$ 38

3: Structural Analysis 40

3.1 Introduction 40

3.2 Neutron and X-ray Diffraction Analyses 45

3.2.1 Experimental 45

3.2.2 Results 49

3.2.2.1 Order and Disorder in the Pyrochlore Structure 60

3.2.2.2 Cation Distribution 68

4: Conclusions 70

5: Future Work 72

6: References 74

List of Figures

1.1 **(a)** A projection of the pyrochlore structure along the a_3 axis for $0 \leq z \leq {}^1/_4$ **(b)** A projection of the pyrochlore cell contents for ${}^1/8-\Delta \leq z \leq {}^3/8+\Delta$ 12

1.2 Graph of x-Ray scattering factors, f, of Y^{3+}, Zr^{4+}, Sn^{4+} as a function of $\sin\theta/\lambda$ 18

2.1 The chemistry of the Pechini Process is depicted [19] 23

2.2 The flowsheet for the preparation of oxides by Anderson[18,19] 25

2.3 The solubility isotherm for the zirconium(IV)-citric acid-water system [7] 31

2.4 **(a)** The thermogravimetric (TG) analysis of a Y^{3+}, Zr^{4+}, Sn^{4} citrate-solution **(b)** The differential thermogravimetric plot (DTG) **(c)** The differential thermal analysis (DTA) 37

3.1 A comparison of the magnitude of the superstructure peaks with those of the substructure in the **(a)** neutron diffraction and **(b)** x-ray diffraction patterns for $Y_2(Zr_{0.2}Sn_{0.8})_2O_7$ 50

3.2 **(a), (b), (c), (d)** Neutron powder diffraction profiles for y=0.2, y=0.4, y=0.6, and y=0.8 respectively 52-53

3.2 **(e), (f), (g), (h)** X-ray powder diffraction profiles for y=0.2, y=0.4, y=0.6, and y=0.8 respectively. .. 54-55

3.3 Variation of the lattice constant of $Y_2(Zr_ySn_{1-y})_2O_7$ with increasing Zr content from neutron and x-ray analyses 59

3.4 A comparison of the change in the x coordinate for O(1) as a function of the mean radius of the cations nominally occupying the B site for $Y_2(Zr_yTi_{1-y})_2O_7$ and $Y_2(Sn_yTi_{1-y})_2O_7$ 61

3.5 Quadratically-decreasing O(1) x-coordinate with increasing amounts of Zr in $Y_2(Zr_ySn_{1-y})_2O_7$ 62

3.6 Neutron diffraction analyses by Heremans [1,2] of $Y_2(Zr_yTi_{1-y})_2O_7$ show the change in anion occupancies as a function of Zr content y 63

3.7 Results of preliminary x-ray studies by Yeo [5,43] showing the change in the occupancies of the anion sites as a function of increasing Zr content, y, in $Y_2(Zr_ySn_{1-y})_2O_7$ 64

3.8 **(a)** X-ray diffraction data of this study showing the change in occupancies of the oxygen ion array as a function of increasing Zr content, y, in $Y_2(Zr_ySn_{1-y})_2O_7$. **(b)** Neutron data showing the change in the occupancies of the anion sites as a function of Zr content in $Y_2(Zr_ySn_{1-y})_2O_7$ 65

3.9 Comparison of the O(1) x-coordinate as a function of average ionic radius of the B site in three solid solution series, $Y_2(Zr_yTi_{1-y})_2O_7$, $Y_2(Sn_yTi_{1-y})_2O_7$, and $Y_2(Zr_ySn_{1-y})_2O_7$ 67

List of Tables

1.1 Definitions of Commonly Used Numerical Criteria of Fit or Residuals (R-values) [50] 16

1.2 Comparison of Ionic Radii, Number of Electrons, and Neutron Scattering Lengths for Ionic Species Present in $Y_2(Zr_ySn_{1-y})_2O_7$ 19

2.1 Heating Schedule for Assaying Stock Solution Samples 36

2.2 TG/DTA Heating Schedule for Citrate Solution Sample 38

2.3 Heating Schedule of the Charred Resin Intermediate to Obtain Fine White Oxide Powder Samples of $Y_2(Zr_ySn_{1-y})_2O_7$ 39

3.1 Neutron Derived Lattice Constants, Atomic Coordinates, Site Occupancies, and Anisotropic Temperature Factor Coefficients for $Y_2(Zr_ySn_{1-y})_2O_7$ 57

3.2 X-Ray Derived Lattice Constants, Atomic Coordinates, Site Occupancies, and Anisotropic Temperature Factor Coefficients for $Y_2(Zr_ySn_{1-y})_2O_7$ 58

3.3 X-ray Derived Lattice Constant, Peak-Shape, and Residuals for the Substructure Peaks in which Cations Contribute only 60

3.4 Cation Distribution from Combined X-Ray and Neutron Analyses 68

3.5 Relative Percent of Total Stoichiometric Amount of Each Cation Distributed in Sites A and B 68

1. Introduction

1.1 Purpose of this Research

Fast-ion conduction is property that is receiving growing attention in recent years because of increasing demands for more diversified and cleaner energy sources. Fast-ion conductors are solid materials displaying ionic conductivities (ranging from 10^{-6} to 4 S/cm) that approach values comparable to those found in liquid electrolytes such as that in an automobile battery [2]. The high ionic conductivities exhibited in these materials are suitable for use as fuel cell electolytes. Ionic conductivity, in contrast to electronic conductivity in which electrons are the charge carriers reflects an ability of ions to freely move through a matrix to conduct electricity. In solid-state materials, this movement of ions in a crystalline or amorphous structure can arise from a variety of diffusion mechanisms. One possible mechanism in an ionic crystalline material, such as a ceramic oxide that is found today in commercial solid oxide fuel cells, is the motion of oxygen ions into "holes" or vacancies in the structure. Establishing a basic understanding of the relationship between crystal structure and conductivity can lead to more rapid optimization of the property for the development of new and improved materials.

This thesis focuses on the structural analysis of a specific fast-ion conducting solid-solution system, $Y_2(Zr_ySn_{1-y})_2O_7$, which are oxide materials with the intriguing $A_2B_2O_7$ pyrochlore structure type. This particular solid solution series was chosen with the hope of reconciling very different results obtained in previous structural studies by Heremans [1,2] and Eberman [3] of $Y_2(Zr_yTi_{1-y})_2O_7$ and $Y_2(Sn_yTi_{1-y})_2O_7$ respectively. The initial interest in structures in the system ($Y_2Ti_2O_7$-$Y_2Zr_2O_7$) was sparked by the conductivity studies by Moon [6]

who found a three order-of-magnitude increase in conductivity (to 10^{-2} S/cm at 1000°C) as Zr substituted for Ti in $Y_2Ti_2O_7$. Subsequently, Heremans [1,2] conducted neutron diffraction analyses of $Y_2(Zr_yTi_{1-y})_2O_7$ solid solutions and showed that substitution of the larger Zr ion for Ti induced progressive disorder in both the cation and anion arrays culminating in a defect fluorite structure at y=0.9. Remarkably, the disorder among the oxygen ions and the mixing between cation sites progressed at very distinct rates. The change in the distribution of oxygen vacancies with composition provided a basis for explaining a 10^3 increase in the corresponding oxygen ion conductivity. The relative size difference between the cations occupying the A and B sites apparently served as the driving force for ordering.

Structural and conductivity studies of the $Y_2(Sn_yTi_{1-y})_2O_7$ solid solution series by Eberman [3] and Yu [5] respectively, were performed to test the hypothesis that relative ionic size determined the state of disorder and, thus, conductivity in pyrochlore-type materials. The results revealed marked contrasts to the titanium-zirconate series. Using compositions with the same average B-site radius as Hereman's samples, Eberman showed a high degree of ordering was present in both the cation and anion arrays for the entire range of solid solution despite the progressively decreasing radius ratio of the cations occupying the A and B sites [3]. Thus, disorder in the stannate series clearly is not subject to the same influence of radius ratio as the zirconates. The nature of a strong Sn-O covalent bond may plays a role in maintaining an ordered structure [3,5].

The interesting question then arises about the kind of disorder that might occur in solid solutions between yttrium zirconate and stannate in view of their diametrically-opposed behaviors . Yeo [4] was the first to perform a preliminary examination of this pseudo-ternary system through x-ray studies of $Y_2(Zr_ySn_{1-y})_2O_7$. The behavior of the series appeared to be similar to that found in $Y_2(Zr_yTi_{1-y})_2O_7$ but her efforts were complicated by difficulties in synthesis of single-phase powders. A second yttrium silicate phase appeared in some of the

samples as a result of the processing technique employed. Yeo investigated samples with compositions where the Zr content, y, was equivalent to 0.2, 0.4, and 0.6. In this report, I have recorded a newly-devised synthesis method after an extensive examination of literature on the Pechini method, and prepared new samples with the compositions of Yeo's work in addition to a sample with y=0.8. Both x-ray and neutron diffraction data were collected and analyzed using the Rietveld method to confirm Yeo's results and revisit the question of disorder in the anion and cation array [43].

In many modern crystalline materials in which doping is advantageous to enhance a particular property (i.e. conductivity) for technological applications, more than two distinct species are found on a single crystallographic site. In our fast-ion conducting pyrochlores, $Y_2(Zr_ySn_{1-y})_2O_7$, three types of cations, Y^{3+}, Zr^{4+} and Sn^{4+}, are distributed over two diffferent crystallographic sites. To determine the exact distribution of the three cation species over two sites, one additional linearly-independent diffraction pattern is necessary for each distinct cation species beyond the number of available sites[37,38,40]. The cation distribution of three species over two sites has never been determined for a pyrochlore oxide. Thus, an additional objective of this paper of general crystallographic interest is the determination of the partitioning of cations in the solid solutions using neutron and X-ray powder-diffraction data in a combined approach for Rietveld structural-analysis. A strong site preference for one of the cation species might well be the factor that could explain the fact that some solid solutions with a given ratio of cation radii tent to disorder whereas others with the same mean sizes do not.

1.2 The Pyrochlore structure

Pyrochlore oxide materials of the general formula $A_2B_2O_7$, where A and B are cations, represent a family of phases identical in structure to the mineral pyrochlore, $(NaCa)(NbTa)O_6F/(OH)$ [41]. Predominantly cubic and ionic, pyrochlore compounds can

have a wide range of chemical substitution at the A, B, and O sites as long as the ionic radius and charge balance are amenable to the specific site. Valences of the A and B sites in many pyrochlores are +3 and +4 respectively or +2 and +5. Vacancies can occur in the A and O sites and result in cation migration within the crystal structure. With a wide range of chemical-substitution and presence of vacancies in its structure, pyrochlore compounds can exhibit numerous physical properties including insulating, fast-ion conducting, semiconducting, paramagnetic, ferro-magnetic, dielectric, piezo- and ferro-electric, and catalytic behavior [10,41].

A superstructure with a lattice parameter twice that of a fluorite-type subcell, the cubic pyrochlore structure, space group Fd3m, is shown in projections along a_3 in Fig. 1.1(a) and 1.1(b). The large cation A^{3+}, coordinated by eight O^{2-} ions, occupies position 16c $\bar{3}$m 000; the smaller cation B^{4+}, surrounded by six O^{2-} ions, occupies position 16d $\bar{3}$m $^1/_2{}^1/_2{}^1/_2$. Fifty-six oxygen anions per cell are found in three crystallographically-independent sites: O(3) in 8b $\bar{4}$3m $^3/_8{}^3/_8{}^3/_8$ is vacant in a fully ordered pyrochlore and would be fully occupied in a fluorite array; O(1) is in 48f mm x $^1/_8{}^1/_8$ and O(2) in 8a $\bar{4}$3m $^1/_8{}^1/_8{}^1/_8$, each tetrahedrally coordinated by two A and two B cations and four A cations, respectively. An ideal position of $x=^3/_8$ for O(1) would describe a regular cubic array of anions. Instead, O(1) relaxes toward the vacant O(3) site and $x>^3/_8$. This probably occurs because of the absence of the otherwise repulsive force of an anion in the 8b position as well as the larger bond distance between O(1) and A^{3+} compared to that with B^{4+} [42].

Factors controlling ordering of pyrochlores have been studied extensively. Ionic radii of the cations, temperature, and stoichiometric deviations are three main parameters that influence the stability of a given pyrochlore [2]. Elevated temperatures cause many $A_2B_2O_7$ pyrochlores to disorder into a non-stoichiometric, defect fluorite structure $(A,B)O_{7/4}$ [1,3]. In early studies of stannate pyrochlores, $A_2Sn_2O_7$, Brisse and Knop [46] suggested that the ratio

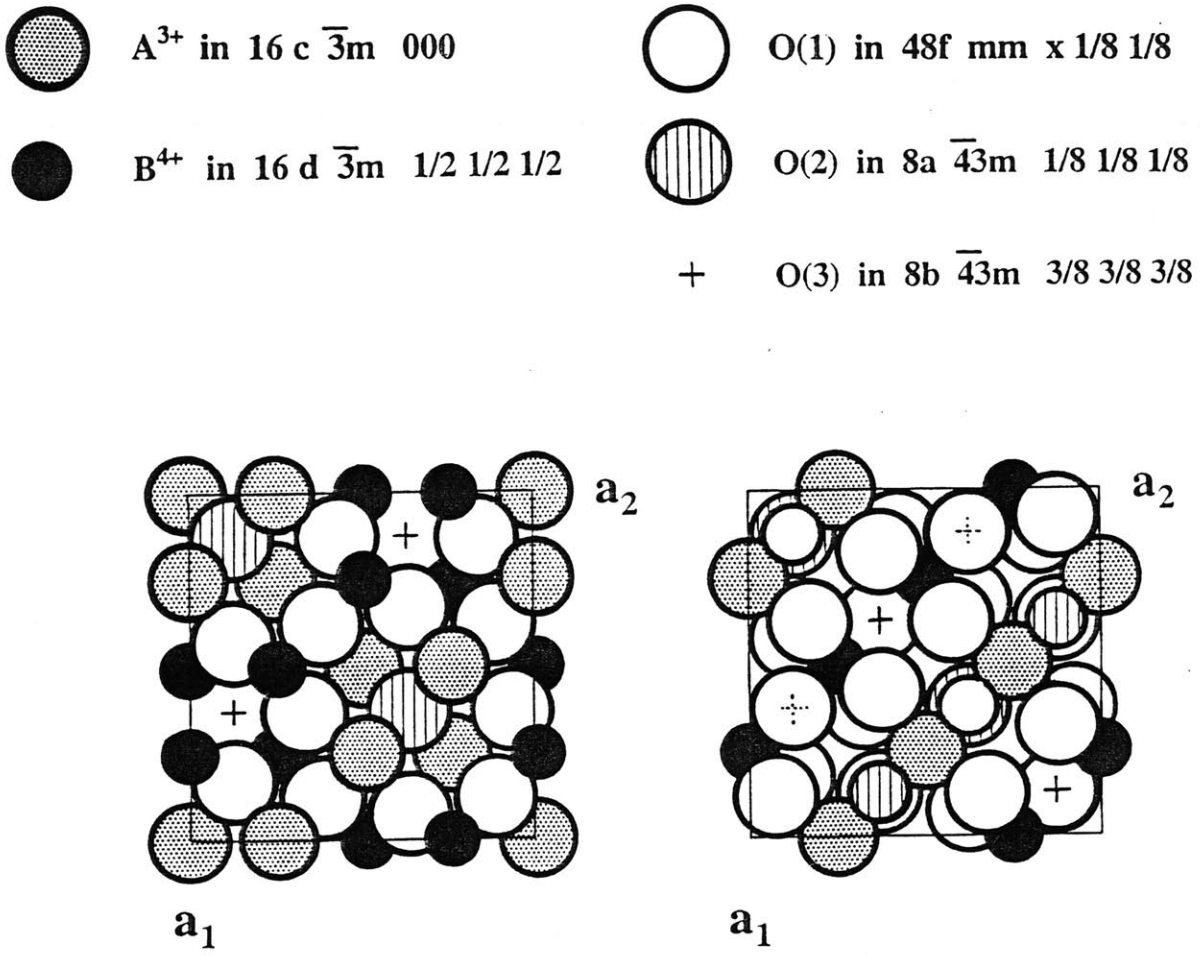

Figure 1.1 (a) *A projection of the pyrochlore structure along the a_3 axis for $0 \leq z \leq 1/4$, showing the cation ordering around the different oxygen ion sites. The depicted O(1) displacement, $\Delta = x - 3/8$ where x is the O(1) coordinate, is 0.462 Å corresponding to $x = 0.4207$ occurring in $Y_2Sn_2O_7$* ***(b)*** *A projection of the pyrochlore cell contents for $1/8 - \Delta \leq z \leq 3/8 + \Delta$, showing the coordination around the cation sites (distorted 8 fold coordination around A^{3+} and 6-fold coordination around B^{4+})*

of the ionic radii of the A^{3+} to the Sn^{4+} ion rather than the chemistry solely determines the stability of the pyrochlore structure. Upper and lower limits of relative ionic radii of the A and B cations (r_{A3+}:r_{B4+}) were proposed as a range for pyrochlore stability. However, more recent systemmatic studies by Kennedy [45] of stannate pyrochlores of the lanthanide elements attributed complete cation and anion ordering to the covalent character of the Sn-O bond [45]. Thus, while the ionic radii can be used as a good initial estimate of the stability of the pyrochlore phase, the chemistry of the individual species must also be considered [3].

The order-disorder transition induced in the pyrochlore crystal structure by solid solution (as opposed to temperature) has also captured the interest of many researchers. As seen in $Y_2(Zr_yTi_{1-y})_2O_7$, this transition is accompanied by a 10^3 increase in the corresponding oxygen ion conductivity[1]. Various models proposed by several researchers of zirconate pyrochlores of the lanthanide elements have offered differing explanations of disordering in the oxygen ion array [1]. One model suggests the evolution of antiphase boundaries during pyrochlore formation. Through electron microscope and computer simulation techniques, Van Dijk [24,29] propounded that pyrochlore formation begins with cluster formation of anions ordering in a fluorite matrix. These clusters take on more pyrochlore character as cations move to the appropriate positions. The pyrochlore domains, embedded in a disordered fluorite structure, grow until the domains touch to form antiphase boundaries. Van Dijk concluded that these antiphase boundaries provide possible pathways for oxygen ion mobility accounting for high ionic conductivity [24]. It is interesting to note, and as will be seen later in Chapter 2 of this report, that the synthesis method common to Hereman's and Van Dijk's samples was the Pechini approach via citrate complexation of metal precursors.

1.3 Complementary Use of Neutron and X-Ray Powder Diffraction

Single-crystal X-ray and neutron diffraction experiments have been the main contributor of detailed understanding of the structures of crystalline materials in past years. With a need for the rapid development of new solid-state materials, growth of single crystals is time-consuming and often extremely difficult or impossible. With recent advances in the development of computer-automated diffractometers to collect digitized data in a step-scan procedure and of the Rietveld refinement method, powder diffraction provides an excellent alternative to single crystal methods for structural analyses [7].

An ideal polycrystalline material or powder can be thought of as an assemblage of a large number of randomly-oriented single crystals [49]. A beam of radiation that is directed at a crystal is diffracted by the set of lattice planes with Miller indices, h,k,l,denoted hereafter as K and proportional to the structure factor F_K, which contains all the information on the structure of a crystal [2]:

$$F_K=\sum_j f_j\, e^{2\pi i(hx_j+ky_j+lz_j)}\, e^{-M_j} \qquad (1.1)$$

where the scattering factors, f, for the jth atom (with fractional coordinates x_j,y_j,z_j), are summed over the unit cell. M_j is the temperature factor which reduces F_K by a factor that depends on the thermal vibrations of the atoms around their equilibrium positions [2].

In powder diffractometry, the randomly-oriented planes of each crystallite in the powder specimen results in a series of diffraction cones whose intensity can be measured by moving a detector along a circle centered on the sample [49]. Details on diffraction theory can be found in a number of sources [48,49]. Generally, two methods are used to extract structural information from powder diffraction data. One technique is to measure the integrated intensities of individual Bragg reflections (after deconvolution of those that overlap)

and convert them to structure factors as one would for a single crystal. However, this method works well only for simple, highly-symmetric structures with minimum peak overlap[7]. The other approach is the Rietveld method in which the entire powder diffraction pattern is used. Each data point is considered an observation. Subsequently, structural parameters, background coefficients, instrumental, and profile parameters are varied in a least-squares procedure until the calculated profile based on the theoretical structure matches the experimental diffraction pattern [7,50].

The best least-squares fit in a Rietveld refinement minimizes the residual, S_y [50]:

$$S_y = \sum_i w_i (y_i - y_{ci})^2 \qquad (1.2)$$

where w_i is $1/y_i$or the weight of the ith observation, y_i is the observed intensity at the ith step, and y_{ci} is the calculated intensity at the ith step [2,50]. The powder pattern can be thought of as an ensemble of individual reflection profiles with an associated peak-height, position, breadth, decaying tails, and an integrated area proportional to the Bragg intensity, I_K, where K represents the Miller indices, h, k, l [50]. The Bragg intensity is proportional to the square of the absolute value of the structure factor $|F_K|^2$ [2,50]. Table 1.1 [50] is an expanded list of several types of residuals (R-values) that are currently used as figures-of-merit in Rietveld analyses. Each R-value uses different criteria to judge the calculated fit of the proposed model to the measured intensities, and indicates if the refinement cycles are proceeding satisfactorily or nearing the end (convergence) [50].

While Rietveld analysis is a useful tool in solving structural problems, site-specific information may be inconclusive from a single powder diffraction pattern as seen in the determination of cation partitioning of several species in the same site (Section 1.1). Therefore, combined use of varied sources for diffraction such as X-rays or neutrons provides insight into crystal structure as well as site-occupancies [47]. Several researchers have

Table 1.1 Definitions of Commonly Used Numerical Criteria of Fit or Residuals (R-values) [50]

$$R_F = \frac{\sum |(I_K(\text{'obs'}))^{1/2} - (I_K(\text{calc})^{1/2})|}{\sum (I_K(\text{'obs'}))^{1/2}} \qquad (\text{'}R\text{-structure factor'})$$

$$R_B = \frac{\sum |I_K(\text{'obs'}) - I_K(\text{calc})|}{\sum I_K(\text{'obs'})} \qquad (\text{'}R\text{-Bragg factor'})$$

$$R_p = \frac{\sum |y_i(\text{obs}) - y_i(\text{calc})|}{\sum y_i(\text{obs})} \qquad (\text{'}R\text{-pattern'})$$

$$R_{wp} = \left\{ \frac{\sum w_i (y_i(\text{obs}) - y_i(\text{calc}))^2}{\sum w_i (y_i(\text{obs}))^2} \right\}^{1/2} \qquad (\text{'}R\text{-weighted pattern'})$$

Here I_K is the intensity assigned to the Kth Bragg reflection at the end of the refinement cycles. In the expressions for R_F and R_B the 'obs' (for observed) is put in quotation marks because the Bragg intensity, I_K, is rarely observed directly; instead the I_K values are obtained from programmatic allocation of the total observed intensity in a 'scramble' of overlapped reflections to the individual reflections, according to the ratios of those reflection intensities in the calculated pattern.

The '*Goodness-of-fit*' indicator, S, is

$$S = [S_y/(N - P)]^{1/2} = R_{wp}/R_e$$

where

$$R_e = \text{'}R\text{-expected'} = [(N - P)/\sum w_i y_{oi}]^{1/2}.$$

The *Durbin–Watson statistic*, 'd', is

$$\text{'}d\text{'} = \sum_{i=2}^{N} (\Delta y_i - \Delta y_{i-1})^2 \Big/ \Delta(\Pi y_i)^2_{i=1}^{N}$$

where

$$\Delta y_i = y_{oi} - y_{ci}.$$

N = the number of profile points
P = the number of refined parameters

employed the combined use of conventional x-ray and neutron diffraction to study cation ordering in superconductor-related compounds [31-34]. Joint synchrotron X-ray and neutron data have also been used to successfully determine the crystal chemistry and electronic structure (valence) of the ions in crystals in addition to the structure as a whole [35-38].

X-rays and neutrons interact with atoms in a crystal differently. X-rays interact with the electrons surrounding an atom. The diffraction effects are, therefore, relatively insensitive to the presence of low atomic number elements early in the periodic table. Scattering power of the atoms also declines with increasing angle because of the size of the electron cloud around an atom is approximately the same as the x-ray wavelength [8,47,58]. The scattering factors for x-rays of cations in our solid solution series of interest, namely, Y^{3+}, Zr^{4+} and Sn^{4+}, are shown in Fig. 1.2 [51]. Notice that $Y^{3+}$and Zr^{4+} with identically 36 electrons have nearly overlapping atomic scattering factors for the entire range of diffraction angles. Thus, distinguishing between these two cations via conventional x-ray diffraction is extremely difficult and especially so for $Y_2(Zr_ySn_{1-y})_2O_7$ given the weak intensity of superstructure peaks as will be discussed later. Sn^{4+} which has 46 electrons may be seen to have a substantially different scattering factor profile.

In contrast to x-rays, neutrons interact with the nuclei of the atoms, and since the nuclear dimensions are three orders of magnitude smaller than the neutron wavelength, point scattering results; thus, neutron scattering factors (also called scattering lengths) are angle independent. The rapid decrease in the scattering factor in x-rays with increasing angle limits the precision of the thermal parameters of the atoms. Hence, neutron data provides more precise thermal parameter values. Because nuclear scattering is dependent on the number of nuclear particles (potential scattering) and neutron absorption by the nucleus (resonnance scattering), neutron scattering lengths vary erratically across the periodic table and between isotopes as well [8,58]. Thus, x-ray and neutron powder diffraction patterns will look

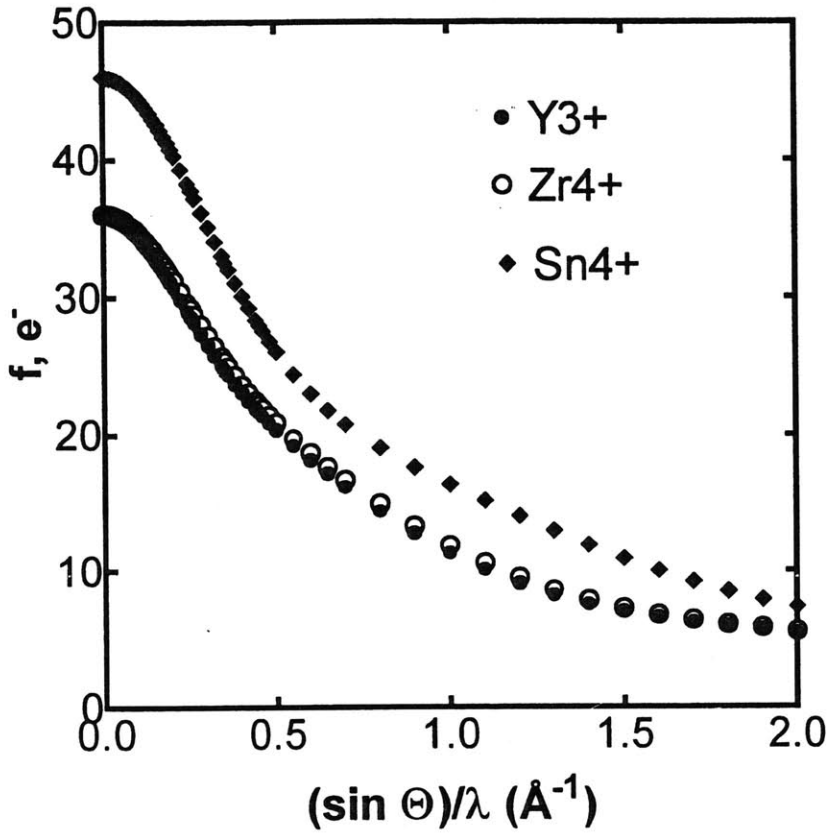

Figure 1.2 *Graph of x-Ray scattering factors, f, of Y^{3+}, Zr^{4+}, Sn^{4+} as a function of $\sin\theta/\lambda$. Values are based on the scattering of the corresponding free ions as listed in the International Tables of Crystallography [51]. Y^{3+} and Zr^{4+}, each with 36 electrons, have nearly overlapping scattering factors over the entire range of 2θ. The lack of scattering contrast between these two species makes them indistinguishable in x-ray diffraction. As will be explained later in Section 3.1, the indistinguishablity will be used to our advantage when determining cation distributions of the three species in two sites.*

different. Table 1.2 lists the neutron scattering lengths, also denoted as b, of each of the constituents in our pyrochlore $Y_2(Zr_ySn_{1-y})_2O_7$:

Table 1.2: Comparison of Ionic Radii, Number of Electrons, and Neutron Scattering Lengths for Ionic Species Present in $Y_2(Zr_ySn_{1-y})_2O_7$

Ion	Coordination Number	Ionic Radius (Angstroms)[9]	Number of Electrons	Neutron Scattering Length (10E-12 cm) [52]
O(2-)	4	1.38	10	0.5803
Y(3+)	8	1.019	36	0.7750
Zr(4+)	6	0.720	36	0.7160
Sn(4+)	6	0.690	46	0.6226

Neutrons, through spin interaction, are also sensitive to magnetic structure. One major disadvantage of neutron diffraction is the need for large sample sizes for powder diffraction, typically 10-20 g in a 5-10 mm diameter cylinder 30 mm long, due to the low scattering cross-section of the neutron [8,38].

As seen in the above discussion, neutron data can provide more precise crystal structures, thermal parameters, and would be more sensitive to anions like oxygens ions than x-ray data. Atoms are mainly identified by their scattering powers relative to other atoms in the structure. Atoms with similar scattering powers will not clearly distinguish the sites these atoms occupy and could be resolved by changing the relative scattering power of the atoms [8]. Thus, analysis of a combined data set, such as neutron and x-ray diffraction data, can solve the problem of atomic or ionic ordering. Williams [8,31,35,58] was one of the first to use both conventional x-ray and neutron diffraction in a simultaneous Rietveld refinement to demonstrate the cation ordering in superconducting $YBa_2Cu_3O_{6+x}$. The use of these two different but complementary data sets resulted in a more tightly constrained refinement and in a more precise structure.

Another useful application of the complementary use of x-rays and neutron diffraction is to address the more difficult problem of atomic site distributions. Williams [32,35] was also the first to use anomolous x-ray and neutron diffraction to study the ordering of three cations among two sites in $Fe_{0.50}Co_{0.48}V_{0.02}$. A minimum of two linearly independent structure factors would be necessary to specify site occupancies [35]. Contrary to previous assumptions that the V occupies both sites randomly or prefers the Fe site, the work by Williams [32] showed through a simultaneous Rietveld refinement of the x-ray and neutron data V preferentially occupies the Co sites .

Haile [44] also addressed the problem of specifying the occupancies of two sites by three different cation species using a slightly different approach. By the introduction of specific constraints on occupancies of various sites in $Y_2(Zr_yTi_{1-y})_2O_7$, Haile proved the need for an additional diffraction experiment to completely specify occupancies of the three cations in two sites [1,2,44]. This report implements the chemical constraints introduced by Haile in neutron diffraction analyses of $Y_2(Zr_ySn_{1-y})_2O_7$, and uses these neutron results in subsequent x-ray Rietveld analyses. Thus, a complementary and combined approach of the two different diffraction data rather than a simultaneous refinement, as used in the work by Williams, is used in this report and will be further discussed in Chapter 3.

2. Synthesis of Pyrochlore Oxide Powders

2.1 Introduction

Considering the previous work done on ionic conductivity and structural analysis for the $Y_2(Zr_yTi_{1-y})_2O_7$ and $Y_2(Sn_yTi_{1-y})_2O_7$ systems, one would imagine that the procedures suitable for synthesis of $Y_2(Zr_ySn_{1-y})_2O_7$ powders would be well understood and documented. On the contrary, protocols for synthesis were typically general recipes and ambiguous. P. Moon [6] gives the more detailed outlines of procedures for preparing gadolinium, titanium, yttrium, and zirconium organic precursors. E. Yeo, in her X-ray analysis of $Y_2(Zr_ySn_{1-y})_2O_7$, was not able to produce single phase powders, but found silicate impurities derived from possible glass flakes introduced in her samples during processing [4]. Attempts to follow the documented procedures in the present study led to failures of either producing a continuously-clear solution of the polymeric cation precursors or a single-phase pyrochlore powder.

This chapter hopes to benefit future students of these interesting fast-ion conducting pyrochlore oxides by providing guidelines on how to prepare a given mixed-cation oxide powder via the Pechini Method. To accomplish this objective, a literature review of past and current uses of the Pechini method for obtaining ceramic oxides was conducted and summarized in the following section. Demonstrating the applicability of these practical pointers, the experimental section proposes a new synthesis scheme for $Y_2(Zr_ySn_{1-y})_2O_7$ which was subsequently utilized for the powders employed in the neutron and x-ray powder diffraction measurements conducted in this study.

2.2 Survey of Ceramic Synthesis utilizing the Pechini Method or other Polymeric Precursor Techniques

In his original 1967 patent, Maggio P. Pechini announced his method for preparing lead and alkaline-earth titanates and niobates to form electrical capacitors [28]. Little did he know that his procedure later would be used and modified by numerous researchers to synthesize a wide range of multicomponent oxides for applications beyond the scope of dielectric materials, and later coined as the "Pechini method" or the "Liquid Mix Process" [18]. The attractive features of the Pechini approach are the ability of preparing complex compositions, homogeneous mixing at the molecular level in solution, control of stoichiometry, and low firing temperatures. Conventional solid state reactions for preparing ceramic oxides require extensive milling and grinding which not only can introduce contaminants detrimentally affecting electrical properties, but also leave room for inhomogenities. Moreover, solid state techniques generally require prolonged and high calcination temperatures while Pechini's process theoretically necessitates substantially lower temperatures because of the presence of self-igniting behavior of organic resins.

The original Pechini method calls for forming polybasic acid chelates from alpha-hydroxycarboxylic acids, such as citric acid, with titanium, zirconium or niobium [28]. Chelation is a complexation process in which a ring forms, in this case to include a metal atom. Citric acid has become the more widely used among the various acids that could be employed because the citrate ion metal complexes tend to be stable. This is due to strong coordination of the two carboxyl and one hydroxyl group of the citrate ion to a metal ion in solution [19]. In the presence of a polyhydroxy alcohol like ethylene glycol, the chelates form an ester. When heated, polymerization of the esters occurs thereby forming an organic matrix through the solution[28]. The extremely high viscosity of the polymeric resins favor low cation mobility

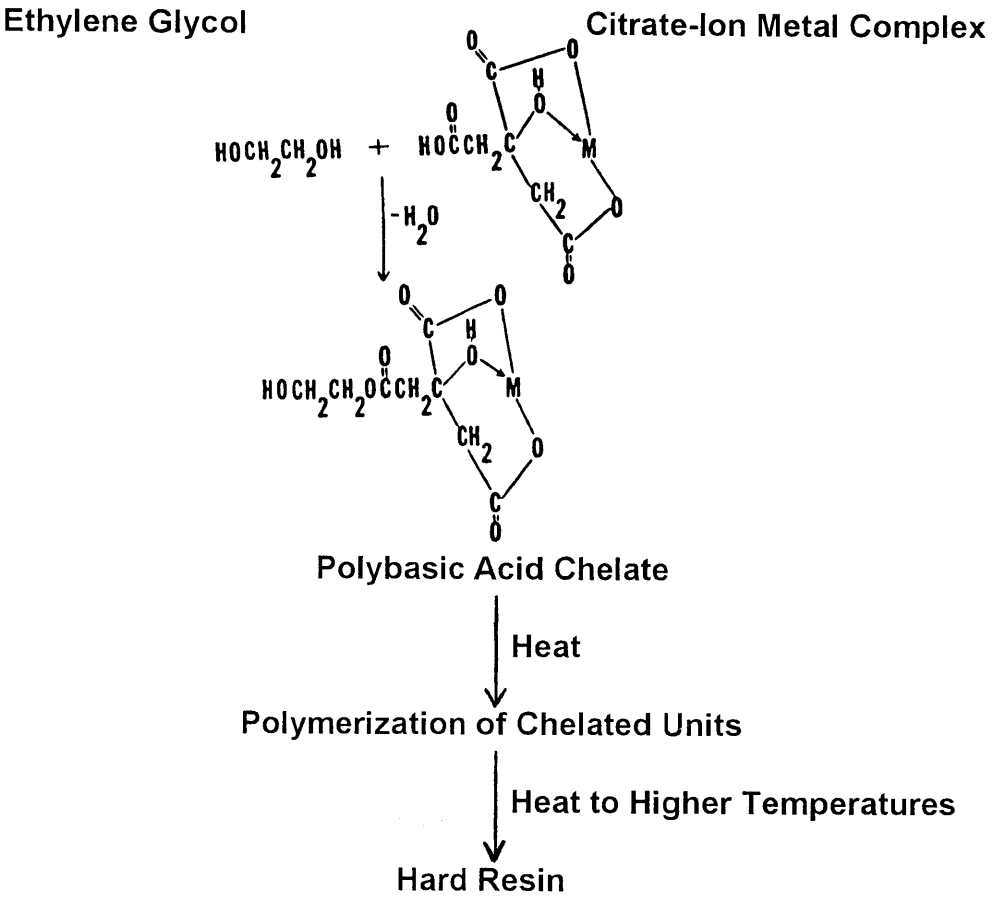

Figure 2.1 *The chemistry of the Pechini Process is depicted [19]. Metal chelates are formed in citric acid solution from strong coordination of the two carboxyl and one hydroxyl group of the citrate ion to the metal ion. In the presence of a polyhydroxyl alchohol, a condensation reaction occurs with the formation of a water molecule. When heated, the hydroxyl ends of the depicted reaction product link (polyesterification) to form a homogeneous solution of metal ions attached to an organic matrix [19,28].*

which helps prevent the different mixed cations from segregating. Upon further heating to remove excess solvent, a transparent solid resin or glass containing the metals in solid solution is formed. Burning off the organic cross-linked network leaves behind fine particulates of the desired multi-metal oxide. Figure 2.1 diagrams the chemistry of the Pechini process [19].

As far as specific quantities of starting materials in the method is concerned, Pechini suggested dissolving one mole of at least one member of the hydrated oxide, alkoxide, and alpha-hydroxycarboxylate of titanium, zirconium, and niobium with 2-8 moles of citric acid and excess ethylene glycol until a clear solution is obtained. Into this solution, 1-1.5 stoichiometric equivalents of one basic metal compound from the group consisting of the oxide, hydroxide, carbonate, and alkoxide of lead and the alkaline earth metals is dissolved [28].

Popularizing this liquid mix technique, Eror and Anderson [18] reported synthesizing over 100 different oxides including chromites, ferrites, cobaltites, manganites, and silicates using variations of Pechini's method. Expanding the types of cationic sources, they proposed using carbonates, hydroxides, isopropoxides, and nitrates. In the synthesis of lead magnesium niobate powders, Anderson, et al. [19] point out that a desirable feature of the Pechini process is that it allows use of a processing temperature as low as 500° C, thus minimizing the volatilization of lead oxide. They reported a procedure in which the organic precursors were mixed with a ratio of 1 g of anhydrous citric acid to 1.5 mL ethylene glycol. A typical flowsheet for their synthesis process is shown in Figure 2.2 [18,19].

Responding to the increasing interest in mixed-cation oxide ceramics, Tai and Lessing conducted systematic studies of the use of polymeric precursors in the Pechini method [11-13]. They asserted that the physical morphology of the final oxide powder is directly related to the

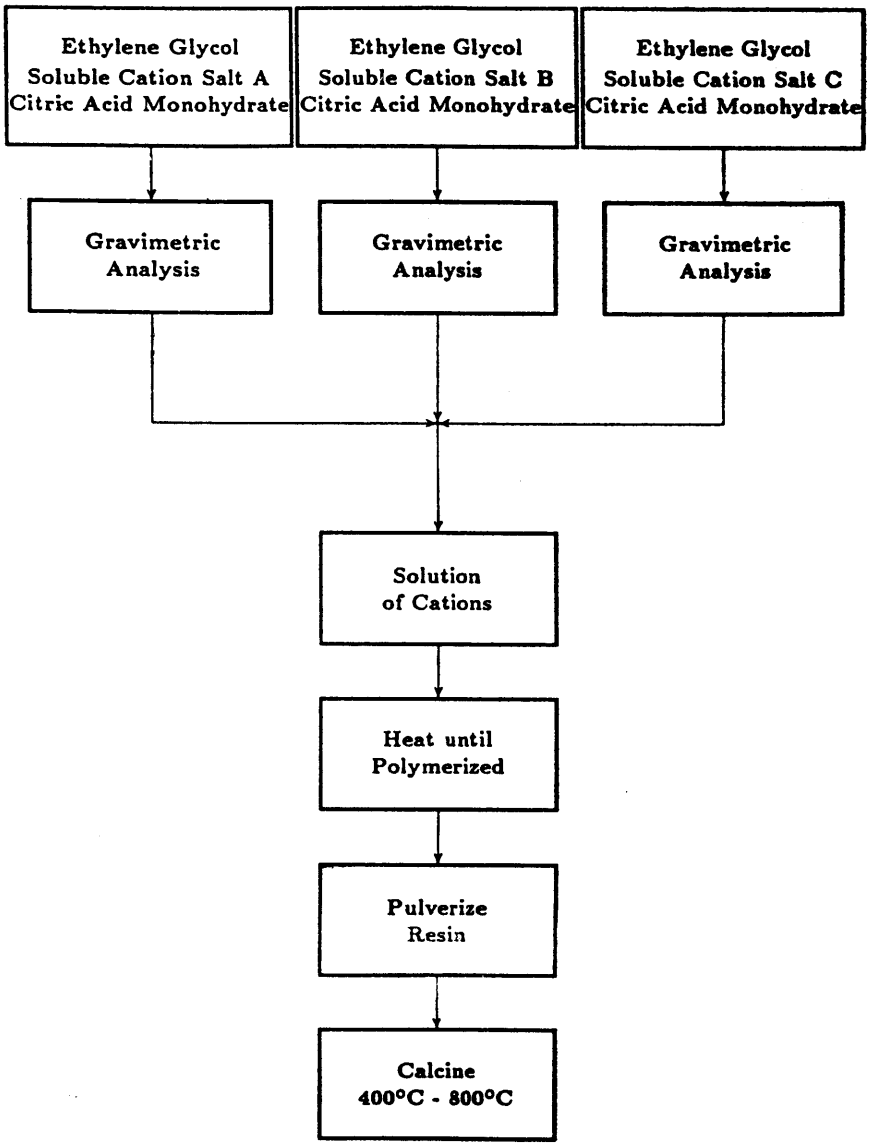

Fig. 2.2 The flowsheet for the preparation of oxides by Anderson[18,19] who first reported the use of a variety of other types of cationic sources besides the ones originally proposed by Pechini. This flowsheet is also adopted for synthesis of pyrochlores in this study.

morphology of the resin intermediate. Maximizing the foaming property of the intermediate resin maximizes, though does not guarantee, the chances of obtaining a single-phase, fine-grained, and non-agglomerated powder. Thus, the optimal "polymeric gel point," that is, the critical citric acid:ethlyene glycol (CA:EG) mixture at which an insoluble polymeric gel forms, was determined to be equimolar or 50:50 through visual characterization of foaming, viscosity measurements, and differential thermal analysis (DTA). They also found that premixing of the citric acid and ethylene glycol at proper ratios prior to addition of the constituent metal nitrate solution reduced the probability of the precipitation which may result from instant changes in pH if pure citric acid is added directly to the solution [12].

In addition, Tai and Lessing found that the water content and the heating schedule during gel setting, charring, and calcination affect the final agglomerate morphology [11,13]. Sufficient water content was found to be necessary for homogeneous mixing, but an amount of water in excess of 100 g per 1 mole of CA-EG polymeric gel retarded the foaming process. The organic precursors, while working as chelating agents, also provide combustion heat for calcination. Use of a mole ratio of organic polymer to nitrate greater than four in their proposed scheme required an excessively high calcination temperature. This resulted in large crystallites that were very strongly agglomerated. A gel:nitrate ratio of 1:1 or 2:1 yielded the resin intermediate of greatest expansion. Ignition can be controlled by lowering the oxygen content of the atmosphere or spreading the resin in a thin layer. Moreover, grinding and shaking the resin prior to calcination facilitated burning off the organic residues [13].

The results of Zhang et al. in their process for the synthesis of dense $YBa_2Cu_3O_{7-x}$ superconducting fibers provide additional insight into the highly-complex chemical reactions of the precursor solutions [15]. They used a 1:4 CA:EG molar ratio, yielding a solution possessing a 3:1 ratio of OH:COOH, and a 1:2.8 metal to carboxylic acid ratio. Desiring a highly-viscous intermediate precursor solution to draw fibers, they found that heating the

solution to a critical temperature of 140° C resulted in esterification between the citric acid and ethylene glycol; therefore, viscosity increased as a function of time and temperature and was independent of the specific cation. A large excess of ethylene glycol terminates the products of the esterification reaction thereby limiting the molecular weight [15].

Choy and Han have modified the Pechini process even further by eliminating all esterification agents such as ethylene glycol in order to minimize particle agglomeration [16-17] . From previous studies, they determined that the ability of the citric acid to chelate with the metal ions is closely related to the kinds of chemical species present in aqueous solution, which in turn are affected by pH, temperature, and concentration. They introduce the idea of theoretical solution modelling to forecast optimum processing conditions through the use of solubility isotherms. By considering the stability domains of all the chemical species as a function of pH versus metal ion concentration, one can determine the minimum pH that may be approached before the onset of the undesirable precipitation of any of the metal hydroxides from the solution. Using metal nitrates or chlorides as their cationic sources, Choy and Han employed their calculated model to predict an optimum pH condition of 6.5, and successively produced single phase $(Pb_{0.92}La_{0.08})(Zr_{0.65}Ti_{0.35})O_3$ [16]. Lee and Fang also use a similar theoretical model to predict the ideal cation:citric acid ratio and pH when using a citrate process from thermodynamic equilibrium constants [26]. In the case of barium ferrite, they found the optimal ratio to be 13:20 at 700° C and a pH of seven.

Modifying the Pechini method further, Liu and Wang use ethylenediamine as an additional chelating agent to fabricate thin films, membranes and coatings of $La_{1-z}Sr_zCo_{1-y}Fe_yO_{3-x}$ on both dense and porous substances [23]. In their work, Liu and Wang found that the most important processing parameter for uniform and crack-free films is the ratio of citric acid to total metal ions--a parameter that they defined as the C ratio. A C ratio greater than 3, in which each metal cation interacts with three molecules of citric acid resulted

in crack-free films. They explained this phenomena by reasoning that the average distance between metal ions decreased in the presence of fewer complexation molecules and, therefore, the interactions among metal ions were stronger. Consequently, metal ion clusters form leading to a nonhomogeneous resin structure. However, too high of a C ratio means a lower packing density of metal ions and greater difficulty in achieving densification during sintering. The quality of the films did not depend on the citric acid to ethylene glycol ratio as mentioned earlier, but the best films had ratios ranging from 1/3 to 1.

Other interesting studies involving the microstructure of the Pechini method may give further insight into the mechanisms of antiphase boundaries formation discussed earlier. In particular, Leite et al. studied the kinetic growth of particles of mixed metal oxides processed by the Pechini method [24]. Their results show that the particle growth is controlled by two different mass-transport systems. Below 800° C, during calcination, surface diffusion leads to filling of necks between nanometric particles. Particle boundaries migrate as neck growth proceeds until the neck becomes the size of a smaller particle. At temperatures above 800° C, the nanometric clusters densify and form elongated grains. This particle growth behavior proved typical of powders processed by the Pechini method and independent of the cations present [24]. Also using a citrate method, van Dijk et al. [29] suggested that pyrochlore domains, 10-100 nm in size, grow in a fluorite matrix and finally form antiphase boundaries. Liete's work [24] would be able to indirectly support such a conclusion.

At this point of the discussion, several points are worth noting as guides to preparing a given mixed-metal oxide. The Pechini method can be tailored to make fine particles, dense fibers, and thin films of a wide array of multi-metal oxides. The modifications to Pechini's basic method that are to be employed depend mainly on the types of metals present in the oxide and, to a certain extent, the desired particle configuration and intended application. The

typical metal precursors used to date have included hydroxides, alkoxides, and carbonates, nitrates, alpha-hydroxycarboxylates, and chlorides [14, 16,19-22].

The first important question when making a mixed metal oxide is to consider the solubility of the metal cations in the citrate solution. Han and Choy [16-17] tackled this problem with the use of solubility isotherms. Alkoxides are highly unstable in the presence of air and hydrolyze in the presence of water forming highly insoluble products. Thus, if using an alkoxide or an easily hydrolyzable compound as a source of cations, non-aqueous based solvents should be used to prevent precipitation of insoluble by-products.

The second factor to consider in using the Pechini method is the desired microstructure. To make fine, non-agglomerated powders, an equimolar citric acid:ethylene glycol ratio has been suggested; for increased density of the powders, a lower ratio should be used, such as the 1:4 ratio employed for making fibers. A "C" ratio or citric acid: cation ratio of 3 has also been reported to promote a more homogeneous resin structure, especially for crack-free films. For x-ray and neutron diffraction studies, a fine non-agglomerated powder would suffice and a CA:cation:EG ratio of 3:1:3 was chosen.

2.3 Experimental Synthesis of $Y_2(Zr_ySn_{1-y})_2O_7$ powders via Polymeric Precursors

2.3.1 Preparation of Stock Solutions

Based on the literature search conducted, a modified technique for making $Y_2(Zr_ySn_{1-y})_2O_7$ was used. Alkoxides were a common precursor used for a source of tin and zirconium in prior syntheses by Yu [5] and Yeo [4]. Not only are they extremely expensive, but more importantly, alkoxides readily hydrolyze in the presence of water, producing insoluble

by-products. The alkoxide precursors were used in an initial attempt to synthesize the samples. When individually-clear citrate stock solutions of yttrium carbonate, tin(II) ethoxide and zirconium n-propoxide were mixed and gradually heated to about 90° C, a milky intermediate solution was observed in the final mixing stages. Although the solution evolved into a clear yellow solution at around 100° C, an alternate synthesis scheme was devised with the thought of preventing such an onset of sudden precipitation. The transient milky solution could have been a result of the temporary adjustment of disparate pH values of the three different stock solutions. Moreover, resin formation using the alkoxides did not seem to yield a completely transparent resin; in fact, a brown slurry seemed to coexist in the resin upon close visual inspection.

Since yttrium carbonate is hydrated, alternative water-soluble metal precursors for zirconium and tin were investigated. According to past studies of zirconium-containing mixed oxides synthesized by the Pechini method, zirconyl chloride had been successively used [14,16,17]. Figure 2.3 depicts the solubility isotherm constructed by Choy and Han for the zirconium(IV)-citric acid-water system [17]. The solubility curve of highly insoluble $Zr(OH)_4$, is superimposed onto the concentration of Zr(IV) ions. Hydroxide precipitation is strongly suppressed in the presence of the complexing citric acid, and can occur above pH=7. Further research was then conducted on possible tin precursors that are stable below pH 7. A logical candidate was tin(II) chloride, $SnCl_2$. Tin (II) chloride is very soluble in water (83.9 g in 100 mL H_2O at 0° C) and stable at low pH or in the presence of strong complexing anions like $CH_3CO_2^-$. In a citric acid solution, the Sn ions can form complexes like $[Sn(C_6H_5O_7)]^-$, $[Sn(OH)(C_6H_5O_7)]^{2-}$ and $[Sn(C_6H_5O_7)_2]^{4-}$ [27]. Unless these low pH or complexation conditions are met, $SnCl_2$ is susceptible to hydrolysis resulting in insoluble tin (II) oxides.

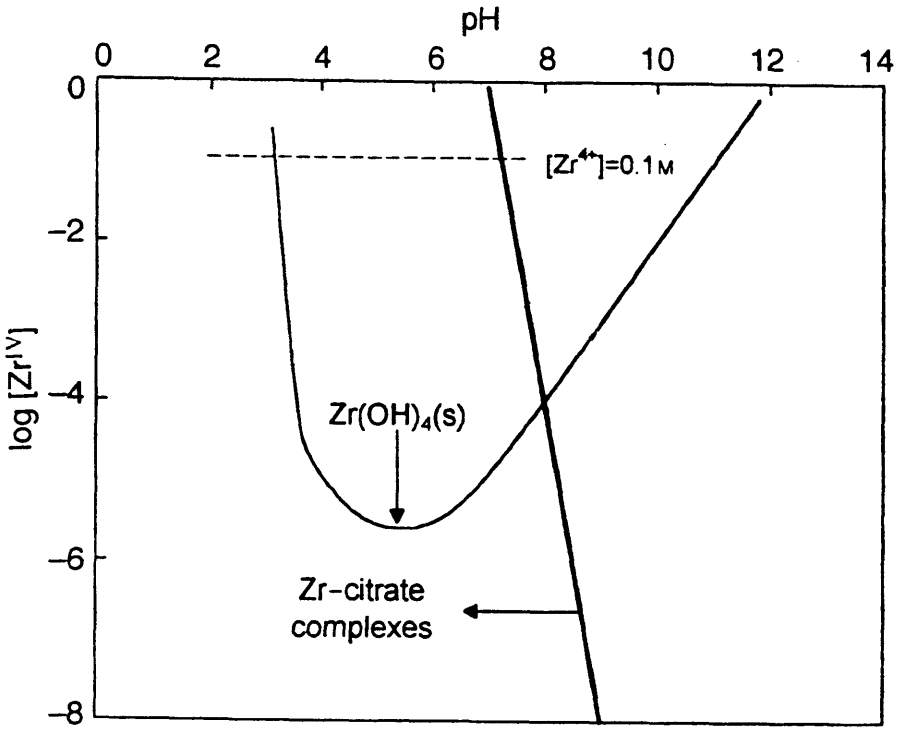

Fig. 2.3 *The solubility isotherm for the zirconium(IV)-citric acid-water system [7]. The solid black line represents the total concentration of soluble zirconium citrates as a function of pH. The curve relates the solubility of $Zr(OH)_4$ (s) in the system. Undesireable precipitation of $Zr(OH)_4$ in the absence of citric acid starts at low pH, but is suppressed in chelate-forming citric acid as noted by the dip in the curve. Below pH=7, zirconium citrates are the dominant species rather than the hydroxy species [7].*

Thus, by carefully considering the properties of the individual cations in choice of precursors, an aqueous based-approach was used. A modified Pechini method as outlined by Anderson et al. [9] and Moon [6] was used where stock solutions of each of the metal cations were prepared. In light of past studies of CA:cation:EG ratios, a 3:1:3 ratio was chosen in order to maximize the amount of chelation to metal ions, provide a fully-foamed and viscous gel to minimize agglomeration and precipitation, and keep the amount of organics to sufficient but not excessive quantities to minimize calcination temperatures. Having a similar pH among solutions is also desireable to minimize precipitation upon combining solutions due to regional variations in pH. In step with Tai and Lessing's suggestion on minimal water content, 0.5 mL of water were used per 1 g of citric acid [12]. Specific procedures for making stock solutions with both the alkoxide or chloride follows.

2.3.1.1 Yttrium Citrate:

To 400 mL of deionized water, 805.3 g of citric acid (anhydrous, ACS, 99.5+%, Alfa) was added and mixed with a magnetic stir bar. Next, after 20 minutes, 234 mL (or 260.2 g since the density=1.1088 g/mL) of ethylene glycol was added. Slow addition of 250 g of $Y_2(CO_3)_3 \cdot 3H_2O$ (Alfa, 99.9%) in 1-3 g increments (roughly a few spatula fulls) was performed over the course of approximately two hours. The solution appeared to be a white-skim-milk like mixture fizzing as a result of the carbonate reacting to form carbon dioxide and water. When left to stir overnight, the solution became completely clear and colorless by the next day. At this point, it is suggested that the solution be assayed (for details on assay procedure see Section 2.3.2 below). The result should be a CA:cation:EG ratio solution of 3: 1: 3.

However, in following Moon's guidelines of subsequent heating to 70° C to ensure

complete dissolution, I heated the solution to 70° C for 4 hours. Polymerization ensued to cause the appearance of fine long fibrous particles and small bubbles. In the future, such a heating step is not recommended. Such a viscous medium is difficult to filter and precisely measure in small quantities for accurate determinations of stoichiometry. Thus, additional ethylene glycol and water were added to decrease viscosity. A total of 12 g of citric acid, 210 mL of ethylene glycol, and 155 mL of pure water was added in this remedial process. This would equate to a CA:cation:EG ratio of approximately 3: 1: 4.9. The final solution was cone filtered over the course of 2-3 days. From experience, use of an aspirator does not significantly speed up the process.

2.3.1.2 Tin Citrate:

A. Aqueous-based approach:

An amount equal to 255.4 g of citric acid was added to 200 mL of pure water. The solution was stirred and heated to 50° C to foster dissolution of the citric acid. Then, 100 g of $SnCl_2 \cdot 2H_2O$ was added to the solution. Two separate layers in the solution were observed at this point: a cloudy mixture on top of a clear bottom solution. Next, 75 mL of ethylene glycol were added to the solution. At this point the solution should be left to stir overnight. A translucent hazy solution resulted, but it became clear and colorless when filtered. It is recommended that the solution be assayed at this point. The result should be a CA:cation:EG ratio of 3: 1: 3.

In an attempt to clear the hazy solution as mentioned above, I added further amounts of citric acid and ethylene glycol. An additional 170.4 g of citric acid and 500 mL of ethylene glycol were added causing no significant change to the solution. The CA:cation:EG ratio used for the final stock solution was 5: 1: 7.7.

B. Alkoxide precursor approach (additional details not mentioned in Yu's work [5]):

To 150 mL of isopropanol, I added 25 g of tin(II)ethoxide ($Sn(OC_2H_5)_2$, Alfa). Stir this peach-colored milky solution for about five minutes. Gradually add 100 g of citric acid over the

course of 2 hours. Increase the temperature to 50°-60° C. An additional 30 mL of isopropanol were added as the solution was thickening and becoming harder to stir. Sufficient time was allowed for chelation to occur; the milky solution became thinner in consistency and resembled skim milk. After about 2 hours, 200 mL of ethylene glycol was added. This turned the mixture to a clear orange solution. The solution was left to stir near the boiling point of isopropanol for 2 hours, filtered, and assayed.

2.3.1.3 Zirconium Citrate:

A. Aqueous-based approach:

To 350 mL of pure water, 250 g of zirconium dichloride oxide ($ZrOCl_2 \cdot 8H_2O$, 99.9%, metals basis, Alfa) was added and dissolved to give a clear solution. To this solution 447.14 g of citric acid was added followed by 130 mL of ethylene glycol. The solution was left to stir overnight. It is suggested that the solution be filtered and assayed at this point. The proportions should result in a CA:cation:EG ratio in the solution of 3: 1: 3.

Like the yttrium citrate solution, this large batch of zirconium citrate was gradually heated to 70° C for 4 hours as suggested by Moon to ensure complete dissolution. However, since both these citrate solutions are readily soluble at room temperature, such a step is unnecessary and even caused polymerization to occur. Fine long fibers were seen in the solution accompanied by the development of an increased yellow/orange color. An additional

50 mL of water and 40 mL of ethylene glycol was added to decrease the viscosity of the solution which was then cone filtered. The final CA:cation:EG ratio of this solution was 3:1:4.

B. Alkoxide precursor approach (additional details added to Moon's original procedures[6]):

Zirconium (IV) n-propoxide ($Zr(OC_3H_7)_4$, Strem Chemicals Inc.) in the amount of 160 g was added to 800 mL of isopropanol and left aside to stir for 20 minutes. To this solution 640 g of citric acid was gradually added. Upon first adding the citric acid, the solution turns yellow and

then becomes increasingly milk white. The mixture was heated to 50° C. Then 800 mL of ethylene glycol was added to the solution upon which it was heated to 100° C as rapidly as possible. The mixture immediately turned into a clear champagne-colored solution. Additional heat should be applied, but for no more than 2 hours to prevent polymerization. The solution was filtered and assayed. Repeated attempts to use zironium (IV) isopropoxide ($Zr(OC_3H_7)_4 \cdot C_3H_7OH$) because of its greater purity over zirconium (IV) n-propoxide (possibly containing up to 0.5-0.9% hafnium) were not successful. Unfilterable, insoluble, white by-products remained suspended in the citrate solution, and gradually settled to the bottom of the reaction vessel over time.

2.3.2 Stock Solution Assay

Each citrate solution was gravimetrically assayed by measuring ideally 10 g quantities in three separate alumina crucibles. The tare and tare+solution weights were recorded. The crucibles were set on a hotplate and heated overnight to 200° C. The crucibles were then put in a box furnace and gradually heated to following the schedule shown in Table 2.1 to prevent bubbling over or loss of sample.

Table 2.1 Heating schedule for Assaying Stock Solution Samples

Starting Temperature(°C)	Ending Temperature (°C)	Ramp Rate (°C/min)	Dwell Time (hrs)
23	200	2	1
200	400	1	3
400	900	2	7
900	105	5	end

The final weight of the crucibles containing the oxide powders was determined and recorded. The oxides were x-rayed to confirm the presence of a single-phase metal oxide. The three sets of results were obtained and averaged to obtain a value for the grams of oxide/g of citrate solution. The estimated error of the assay ranged from 0.01-0.02%. These results were used to determine the weight of stock solution necessary to provide a given weight-fraction of oxide for a solid solution of desired stoichiometry.

2.3.3 Mixing Stock Solutions for Multi-Metal Compositions

Based on the results of the assay, a balance was used to weigh a 2000 mL beaker containing each of the citrate solutions in correct stoichiometric proportions. Crystallizing dishes can be used if a smaller sample size is required. The multi-metal citrate solutions were left to stir overnight to ensure homogeneity.

2.3.4 Thermogravimetric Analysis (TGA/DTA)

To set up an appropriate temperature profile for calcination, thermogravimetric analysis (TGA) and differential thermal analysis (DTA) was conducted for the citrate solution corresponding to $Y_2(Zr_{0.2}Sn_{0.8})_2O_7$. Measurements were taken under ambient conditions on a Seiko Thermal Analyzer (TG/DTA 320). Based on previous experience with citrate solutions and knowledge of the the processing temperature employed [3, 6] the heating schedule for the sample listed in Table 2.2 was used in hopes of observing chemical transitions at each of the steps.

Figure 2.4

(a)*The thermogravimetric (TG) analysis of a* Y^{3+}, Zr^{4+}, Sn^{4} *citrate-solution that would result in* $Y_2(Zr_{0.2}Sn_{0.8})_2O_7$ *when all the organic residues are removed. Continual weight loss (in mg) is noted at temperatures extending to 1450°C.*

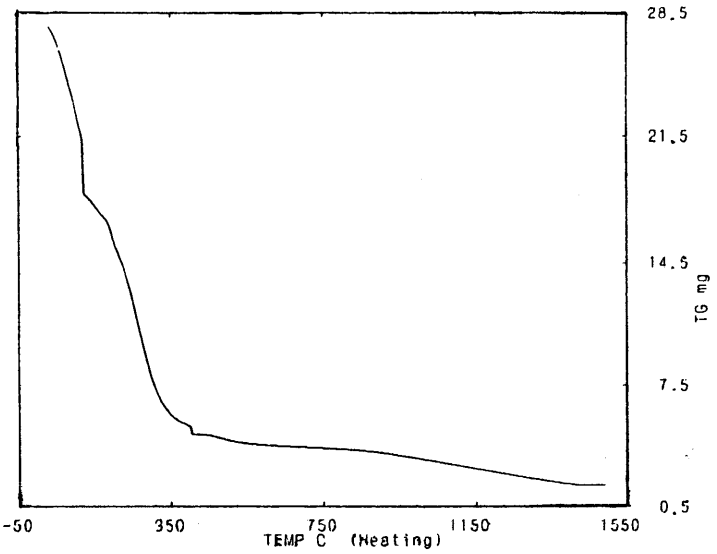

(b) *The differential thermogravimetric plot (DTG) locates peaks in regions of the most significant changes in weight, namely, 260-400° C during the burn-off of organics. The sharp peak located around 200° C is marks the boiling point of ethylene glycol, and signals the elimination of the excess.*

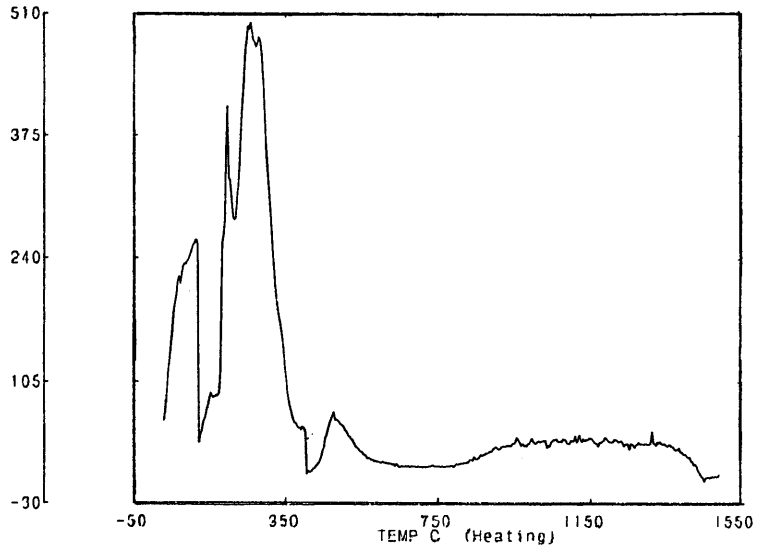

(c) *The differential thermal analysis (DTA) represents the energy, expressed in microvolts, absorbed or released in the reaction. The broad endothermic peak confirm that decomposition of the citrate to the oxide is not complete at temperatures as high as 1450°C.*

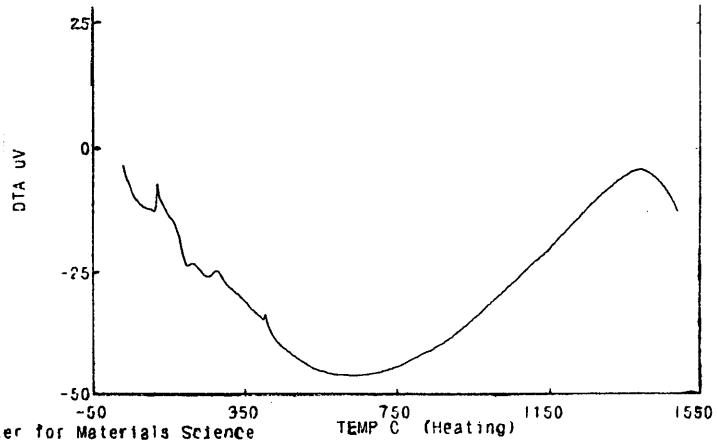

Table 2.2: TG/DTA Heating Schedule for Citrate Solution Sample

Starting Temperature(°C)	Ending Temperature (°C)	Ramp Rate (°C/min)	Dwell Time (hrs)
22	120	3	0.5
120	170	3	0
170	400	5	1
400	1500	10	0

Figure 2.4(a) is a TGA plot of the change of weight as a function of temperature that reveals continual weight loss of weight through 1450° C. Figure 2.4(b), the differential thermogravimetric plot (DTG), shows a sharp spike at around 200° C which is most probably the point where the excess ethylene glycol evaporated (b.p.198°C). The most significant change in weight from 260°C- 400° C occurs from the burn-off of organic residues. The plateau beginning at 750° C and dropping off at 1450° C seems to indicate that decomposition to the pure oxide is not complete until 1450° C. The results of the DTA in Figure 4.4(c) confirm this fact by showing a broad endothermic curve throughout the heating schedule.

2.3.5 Preparation and Processing of Metal Citrate Solutions for $Y_2(Zr_ySn_{1-y})_2O_7$

Using the newly devised solution scheme for preparing stock solutions of the individual metals, a small 1 g sample of $Y_2(Zr_{0.2}Sn_{0.8})_2O_7$ was prepared to test the procedure and confirm the presence of the pyrochlore phase. The microscaled experiment indicated no signs of precipitation during resin formation. Moreover, X-ray diffraction of the final oxide indicated the expected pyrochlore superstructure peaks.

Upscaling to larger batches of 38 g samples of $Y_2(Zr_ySn_{1-y})_2O_7$ where y=0.2, 0.4, 0.6, and 0.8, the mixed metal citrate solutions were measured in the appropriate calculated amounts placed in 2000 mL beakers and weighed on a scale. The solutions remained clear throughout

an overnight mixing at room temperature. However, when gradually heated to 120° C, white precipitate appeared suspended in the solution. Contrary to the results of a smaller sample size, the sudden precipitation in a large batch could be a result similar to that seen for the alkoxides where sudden changes or pH or oxidation conditions resulted in precipitation. However, unlike the synthesis technique using the alkoxides, in which the multi-metal citrate solutions eventually turned into a clear yellow viscous media, the mixture did not cease to have some visible white precipitate suspended in the gel. Thus, the onset of precipitation of the aqueous-based citrates seem to evolve even sooner (during polymerization) than that of the alkoxides which evolved later during the resin formation. The resin was charred to form a tough black mass, and further burned to obtain a grey-white powder.

The powder was then transfered to alumina crucibles and heated to 400° C for 24 hours in a box furnace. After slightly mixing and very modestly grinding the calcined powder, the samples were transferred to a high temperature furnace and further heated treated at 850° C for two hours followed by an equilibration at 1500° C for 30 hours. Following this, the samples were immediately air quenched. The final samples were fine white powders with a faint-pink tint. Table 2.3 summarizes these heating steps and the heating rates employed for the entire solid solution series.

Table 2.3 Heating schedule of the Charred Resin Intermediate to Obtain Fine White Oxide Powder Samples of $Y_2(Zr_ySn_{1-y})_2O_7$

Starting Temperature(°C)	Ending Temperature (°C)	Ramp Rate (°C/min)	Dwell Time (hrs)
23	170	10	0.2
170	400	5	24
	Transfer powders to a High Temperature Furnace		
23	850	8	2
850	1500	10	30
1500	23	20	end

3. Structural Analysis

3.1 Introduction

According to Buerger [53,54], by suppressing certain symmetry operations in a simple atomic arrangement, a derivative structure is formed. Four mechanisms or combinations thereof are possible: ordered substitution, ordered omission, "stuffing" in which an extra atom is positioned interstitially, and distortion. A special type of derivative structure is the superstructure in which a translational symmetry operation is suppressed. Buerger proposed that such superstructures should be analyzed to advantage as the sum of the substructure, that is the average scattering density in the structure, and the complement structure (the function that must be added to the substructure to produce the scattering density in the true superstructure)[1,54]. The pyrochlore structure is a superstructure of a fluorite array of atoms. The diffraction pattern of pyrochlore would thus consist of a strong set of intensities attributed to the average fluorite substructure, and the weaker superstructure intensities from the complement structure. These superstructure intensities contain all the information on the ionic ordering and anionic displacements that form the pyrochlore superstructure [1].

Several challenges arise when analyzing pyrochlore superstructures. Since disorder occurs on both the anion and cation arrays, occupancies of all sites are unknown in an partially disordered pyrochlore. Moreover, the scale factor, which relates observed and calculated intensities in the least-squares Rietveld analysis, is highly correlated to structural parameters including occupancies, temperature factors, and displacement of atoms from ideal substructure positions [1]. In addition, the relatively small differences in scattering lengths and numbers of electrons present in our multi-metal oxide system, $Y_2(Zr_ySn_{1-y})_2O_7$, leads to extremely small superstructure intensities, that weaken further as the structure progressively disorders.

Taking advantage of the fact that all ions occupy special position in the space group, Heremans [1,2] devised a systemmatic determination of key features of the pyrochlore structure through initial deletion of portions of the diffraction pattern. Details of her methodology are described elsewhere [1,2], but the basic four steps, which were also employed in this study for both neutron and x-ray diffraction profiles, are as follows:

(1) Deletion of all but those subcell reflections to which the cations solely contribute permits a good estimation of the scale factor, lattice parameter, instrumental parameters (zero point, peak shape, background) and isotropic temperature-factor coefficients for the cations.
(2) Fixing the value of the scale factor, one then deletes all but the superstructure reflections to which the oxygen ions make contributions and makes a preliminary determination of the x-coordinate for O(1), occupancies and temperature-factor coefficients for the anions.
(3) Inclusion of all the superstructure reflections and refining the cation and oxygen parameters results in full description of the complement structure.
(4) Restoring all the subcell reflections would normally improve agreement between calculated and observed patterns; however, the presence of a coexisting fluorite-like phase in Hereman's $Y_2(Zr_yTi_{1-y})_2O_7$ as well as the solid solution series of this study exacerbated the residuals from inclusion of the entire pattern. Another problem that arises is that the superstructure peaks may have different shapes than the substructure reflections if the former are influenced by antiphase domains or the latter peaks include a contribution from a fluorite phase with slightly different lattice constant.
In this study's structural analysis of $Y_2(Zr_ySn_{1-y})_2O_7$, steps 1-3 were the general strategy employed in the neutron diffraction data. Step 2 was skipped for x-ray data refinement because superstructure reflections only contributed by the oxygens, unlike the neutron data, could be barely distinguished from the background. Thus, oxygen parameters derived from the neutron analyses were used in the x-ray analyses.

The implemention of hard constraints on site occupancies proposed by Haile [44] will be a crucial step in solving cation distributions in the combined analyses. Rietan [39,52] and Refine are the only two Rietveld-analysis programs of which the author was aware of that enabled the user to write constraints with more than one independent variable. Refine, a program of Rietveld as modified for the National Institute of Standards and Technology multidetector diffractometer by Prince [44,55,56] is only able to analyze neutron data. This study uses the latest version of Rietan (Rietan 97-Beta) [52] which is a fairly new software package that can be downloaded from the internet with no cost to the user. While Rietan does not allow for simultaneous refinement of multiple data sets like GSAS [57] (General Structural Analysis Software used by Williams [31,32] in his simultaneous x-ray and neutron studies), Rietan has many advantages including linear and non-linear constraints, a stable automatic-convergence to a minimum of the weighted sum of residuals using complex algorithms in non-linear least-squares procedures, various peak-shape functions, an easy input manner, and several kinds of formats for graphical data [52].

Although mentioned elsewhere [1,2,44], the constraints first introduced by Haile will be recapitulated in this section for clarity and understanding by the reader as these constraints are often referred to in later sections of this Chapter. To start off with the simplest constraint, the connection between oxygen site occupancies in pyrochlore is straighforward since only one scattering length is involved [1,2,44]:

$$48N^1_O + 8N^2_O + 8N^3_O = 56 \qquad (3.1)$$

where N^1_O is the fractional occupancy of the oxygen in the O(1) site. Rearrangement of this equation defines N^1_O and N^2_O as the independent variables:

$$N^3_O = 7 - 6N^1_O - N^2_O \qquad (3.2)$$

The constraints imposed on the cations are less obvious. A single diffraction experiment with our system, $Y_2(Zr_ySn_{1-y})_2O_7$, fails to reveal the exact distribution of the three cations in two crystallographically distinct sites, A and B. In our neutron diffraction studies, only the effective scattering lengths, b_A and b_B, of sites A and B can be determined:

$$b_A = N^A_Y b_Y + N^A_{Zr} b_{Zr} + N^A_{Sn} b_{Sn} \tag{3.3}$$

where N^A_i is the fractional occupancy of site A by species i [1,44]. On the other hand, the scattering length of site B is not independent, but constrained stoichiometrically:

$$b_A + b_B = b_Y + y b_{Zr} + (1-y) b_{Sn} \tag{3.4}$$

Common structural analysis programs like GSAS, Refine, or Rietan only allow for site occupancy refinement as opposed to the scattering lengths of the sites. This obstacle was overcome by assigning only one cation species such as Y to site A, and then refining the occupancy of the A site. This result yields the scattering length of the A site [2]:

$$b_A = N^A b_Y \tag{3.5a}$$

$$= N^A_Y b_Y + N^A_{Zr} b_{Zr} + N^A_{Sn} b_{Sn} \tag{3.5b}$$

As $b_Y > b_{Zr} > b_{Sn}$ (Table 1.2), it follows that $N^A \geq 1$. Moreover, relation (3.4) can be rearranged to become [2]:

$$b_B = [b_Y + y b_{Zr} + (1-y) b_{Sn}] - b_A \tag{3.6a}$$

$$= [b_Y + y b_{Zr} + (1-y) b_{Sn}] - N^A b_Y \tag{3.6b}$$

and arbitrarily assigning the scattering length of Sn to the B site, it follows that:

$$b_B = N^B b_{Sn} \tag{3.7a}$$

$$N^B = [b_Y + y b_{Zr} + (1-y) b_{Sn}]/b_{Sn} - N^A b_Y/b_{Sn} \tag{3.7b}$$

Therefore, by treating N^A as the independent "occupancy", N^B becomes a dependent variable, and equation 3.7b is the hard constraint employed in the refinement program which can also be expressed as:

$$N^B = K_1 - K_2 N^A \tag{3.7c}$$

where K_1 and K_2 are constants equivalent to the calculated value of the coefficients in equation 3.7b. Additionally, assuming that both A and B sites have unit occupancy, the following relations are also established:

$$N^A_Y + N^B_Y = 1 \tag{3.8}$$

$$N^A_{Zr} + N^B_{Zr} = y \tag{3.9}$$

$$N^A_{Sn} + N^B_{Sn} = 1 - y \tag{3.10}$$

In total, five equations are given, but six unknown site occupancies exist [1,2,44]. Thus, an additional x-ray diffraction experiment is conducted to provide the missing information.

As noted previously in Chapter 1, the number of electrons associated with $Y^{3+}$and Zr^{4+} are identically 36. Hence, these two species are virtually indistinguishable in X-ray diffraction. This fact is exploited by solving the site occupancies as a two site, two cation problem by employing only scattering factors for Sn^{4+} and (arbitrarily) Y^{3+} in the calculations. The following site occupancy constraints are introduced in the x-ray analyses assuming that A and B sites have unit occupancies:

$$N^A_{Sn} + N^A_Y = 1 \tag{3.11a}$$

$$N^A_{Sn} + (1-N^A_{Sn}) = 1 \tag{3.11b}$$

$$N^B_{Sn} + N^B_Y = 1 \tag{3.12a}$$

$$((1-y)- N^A_{Sn}) + (y + N^A_{Sn}) = 1 \tag{3.12b}$$

Therefore, the average scattering factors at each cation site can be written as:

$$f_A = N^A_{Sn} f_{Sn} + (1 - N^A_{Sn}) f_Y \quad (3.13)$$

$$f_B = ((1-y) - N^A_{Sn})\, f_{Sn} + (y + N^A_{Sn})\, f_Y \quad (3.14)$$

With all these careful considerations in mind when refining the pyrochlore structure, analysis of $Y_2(Zr_ySn_{1-y})_2O_7$ can begin.

3.2 Neutron and X-ray Diffraction Analyses

3.2.1 Experimental

Neutron diffraction data were collected at ambient conditionswith the 32-detector High Resolution Powder Diffractometer at the Research Reactor at the National Institute of Standards and Technology . The diffraction profiles were collected in steps of 0.05° 2θ for the range of 3.0°-168° 2θ using 1.5402 Å thermal neutrons monochromated by reflection from (311) of a copper single crystal. The volume of the NIST cylindrical sample holder was 9.7096 cm^3 with an inner radius of 0.78 cm. Approximately 15 g of sample were used for each of the measurements. The cylindrical configuration of the sample requires that absorption be corrected as a function of θ_i, the diffraction angle at the *i*th step, during the refinement of the data [3]. Rietan uses an absorption correction factor, $A(\theta_i)$, based on the user's input of the radius of the sample holder r_c and packing density of the sample [52]:

$$A(\theta_i) = \exp\left[(1.7133 - 0.0368\sin^2\theta_i)\mu r_c - (-0.0927 - 0.3750\sin^2\theta_i)(\mu r_c)^2\right] \quad (3.15)$$

The linear absorption coefficient, μ, is calculated from the packing density inputted by the user. Since the packing density of the sample could not be precisely determined because of the unique sample holder employed at NIST, all the samples were estimated to have a packing density of 1.545 g/cm^3, based on an approximate mass of 15 g per sample. Based on calculations using the function of the absorption correction factor employed in Rietan, a discrepancy as great as 50% of the linear absorption coeefficent μ in the sample with the highest absorption in our solid soltuion series (y=0.2 since Sn has a higher absorption cross section than Zr), would still result in relatively small systemmatic source of error. Namely, at low diffraction angles, the absorption correction factor would vary $\pm$2E-06, and at high angles, the correction factor would vary $\pm$0.004. A 10% discrepancy in μ would decrease the margin of error in the absorption correction factor further by an order of magnitude in both low and high diffraction angle regions.

X-ray diffraction data were provided by a Rigaku RU300 18 kW rotating anode generator using Cu Kα radiation (λ_{CuKa1}=1.54051 Å, λ_{CuKa2}=1.54433 Å). The diffracted beams were monochromated from the (002) reflection of graphite. A 0.3 mm receiving slit before the detector, a 1° divergence slit for the beam incident on the sample, and a 1° receiving slit after the monochromater were used. The powders were ground with the addition of sparse amounts of acetone (as a drying lubricant) in an agate mortar and were mounted on a glass slide. Intensity data were collected from 11°-154° 2θ with a step size of 0.03° 2θ, and with a total count-time of 200 minutes per sample for each sample in the solid solution series where y=0.2, 0.4, 0.6, and 0.8. Prior to the scans of the samples, NIST certified Si and LaB_6 standards were measured with the same step size, but over a shorter 20-minute count-time. The Si standard provided the zero-point of the diffractometer, and the LaB_6 standard provided sharp, well-defined peaks for instrumental peak-shape parameters (to be used later in the refinement) that have no functional dependence on the sample [3].

Rietveld analyses were performed using the latest PC versions of Rietan (FAT-Rietan 97beta)[6]. For the neutron diffraction data, a total of 29 adjustable parameters were used in the model. The 15 structural parameters included a scale factor, lattice constant, the O(1) x coordinate, three site occupancies (A, O(1), O(2)), and 9 temperature factor coefficients. As previously mentioned, hard constraints were employed to evaluate the dependent occupancies of B and O(3). The species designated to the B site is arbitrary, and the constant values K_1 and K_2 of the hard constraint (equation 3.7c) was adjusted accordingly. In this study, Sn^{4+} was assigned to the B site for y=0.2 and 0.4; Zr^{4+} for y=0.6; and an imaginary species ($Zr_{0.8}Sn_{0.2}$) for y=0.8. The remaining 14 instrumental variables were the zero-point in 2θ, 8 background parameters, and 5 peak-shape parameters, U, V, W, X, Y. The background function used in Rietan is approximated by a finite sum of Legendre polynomials $F_j(x_i)$, as first expressed by Abramowitz and Stegun [52,60], orthogonal relative to integration over the interval [-1,1]:

$$y_{bi} = \sum_{j=0}^{11} b_j F_j(x_i) \tag{3.16}$$

where b_j are the background parameters to be refined in the Rietveld analysis, and the variable x_i is the diffraction angle 2θ, normalized between -1 and 1 [52]:

$$x_i = \frac{2\theta_i - \theta_{max} - \theta_{min}}{\theta_{max} - \theta_{min}} \tag{3.17}$$

The profile or peak-shape function employed in Rietan is a slightly modified pseudo-Voigt function of Thompson, Cox and Hastings [52,59]. A convolution of a Lorentz (L) and Gauss (G) function, the Voigt function is approximated by a linear combination of the two functions [52]:

$$\phi(\Delta 2\theta) = \eta\phi_L(\Delta 2\theta) + (1-\eta)\phi_G(\Delta 2\theta) \tag{3.18a}$$

$$= \eta \frac{2}{\pi H_k}[1+4(\Delta 2\theta/H_k)^2]^{-1} + (1-\eta)\frac{2(\ln 2)^{1/2}}{(\pi)^{1/2}H_k} \exp[-4\ln 2((\Delta 2\theta)/H_k))^2] \tag{3.18b}$$

where:

$$\eta = 1.36603(H_{kL}/H_k) - 0.47719((H_{kL}/H_k))^2 + 0.11116((H_{kL}/H_k))^3 \tag{3.19}$$

and:

$$H_k = (H^5_{kG} + 2.69269H^4_{kG}H_{kL} + 2.42843\,H^3_{kG}H^2_{kL} + 4.47163H^2_{kG}H^3_{kL} + 0.07842H^4_{kG}H^5_{kL})^{0.2} \quad (3.20)$$

In the above equations 3.17a-3.19 [52], $\Delta 2\theta = 2\theta_i - 2\theta_k$ (*i* is the step number; *k* is the reflection number; $2\theta_i$ is the diffraction angle at the *i*th step; and θ_k is the Bragg angle for the *k*th reflection), ϕ_L is the normalized Lorentz function, ϕ_G is the normalized Gauss function, η is the fraction of the Lorentzian component, and H_k is the full-width-at-half-maximum (FWHM) of ϕ_L and ϕ_G. H_{kL} and H_{kG} are the FWHM of the Voigt function for the Lorentzian and Gaussian components respectively [52].

The variance σ^2 of the Gaussian component can be expressed as:

$$\sigma^2 = U\tan^2\theta_k + V\tan\theta_k + W + P\sec^2\theta_k \quad (3.21)$$

where:

$$H_{kG} = (8\sigma^2 \ln 2)^{1/2} \quad (3.22)$$

Therefore, U, V, W are three peak-shape parameters describing the Gaussian character, and P is the Scherrer coefficient for Gaussian broadening but is not used as an adjustable parameter in this study [52,61]. Variables V and W depend solely on the instrument and not the sample. The Lorentzian contributions to the profile parameters are X, Y, X_e, and Y_e related in the expression:

$$H_{kL} = (X + X_e\cos\varphi_k)\sec\theta_k + (Y + Y_e\cos\varphi_k)\tan\theta_k \quad (3.22)$$

The first part of the expression proportional to $\sec\theta_k$ is associated with crystallite-size broadening. The second part proportional to $\tan\theta_k$ is assoicated with Lorentian microstrain broadening. X and Y are isotropic-broadening coefficients while X_e, and Y_e are anisotropic-broadening coefficients, and φ_k is the angle between the scattering vector and an anisotropic broadening axis [52]. Only X and Y were used as adjustable parameters in this

study. Isotropic thermal factors were assigned to all atoms in the early stages of refinement and later replaced with anisotropic terms.

For the x-ray diffraction data, structural parameters were identical to those used for the neutron data except that the occupancy of O(2) was fixed for y=0.2, 0.4, and 0.6 in the later cycles of the refinement for an improved fit. The zero-point, peak-shape parameters V and W (which solely depend on the instrument), and Lorentz-polarization correction factor as determined by Eberman [3] were fixed at the refined values obtained for these parameters using the NIST-certified Si and LaB_6 standards diffraction profiles measured prior to the solid-solution samples. The remaining instrumental parameters included three peak-shape parameters, U,X,Y, 8 background parameters, specimen displacement, and specimen transparency.

The general refinement approach for both sets of data was outlined earlier in this chapter according to Heremans [1,2]. When the final step of including all the substructure peaks was employed, the dramatic increase in residuals and shift in to a larger lattice parameter, signaled the coexistence of a fluorite-like phase as seen in the $Y_2(Zr_yTi_{1-y})_2O_7$ series. Antiphase boundaries in diffraction patterns are characterized by broadening the superstructure lattice points in reciprocal space, but integrated intensities remain unaffected [2]. The peak shapes employed for the superstructure were incommensurate with the substructure, since the former tends to be broader in shape. Thus, reported values are associated with only the superstructure peaks. Other useful guidelines in the refinement process can be found in work by Eberman [3] and Young [50].

3.2.2 Results

Figure 3.1 (a) and (b) depict low-angle regions of neutron and x-ray powder diffraction patterns for the y=0.2 sample. Since the wavelengths of the thermal neutrons and the x-ray

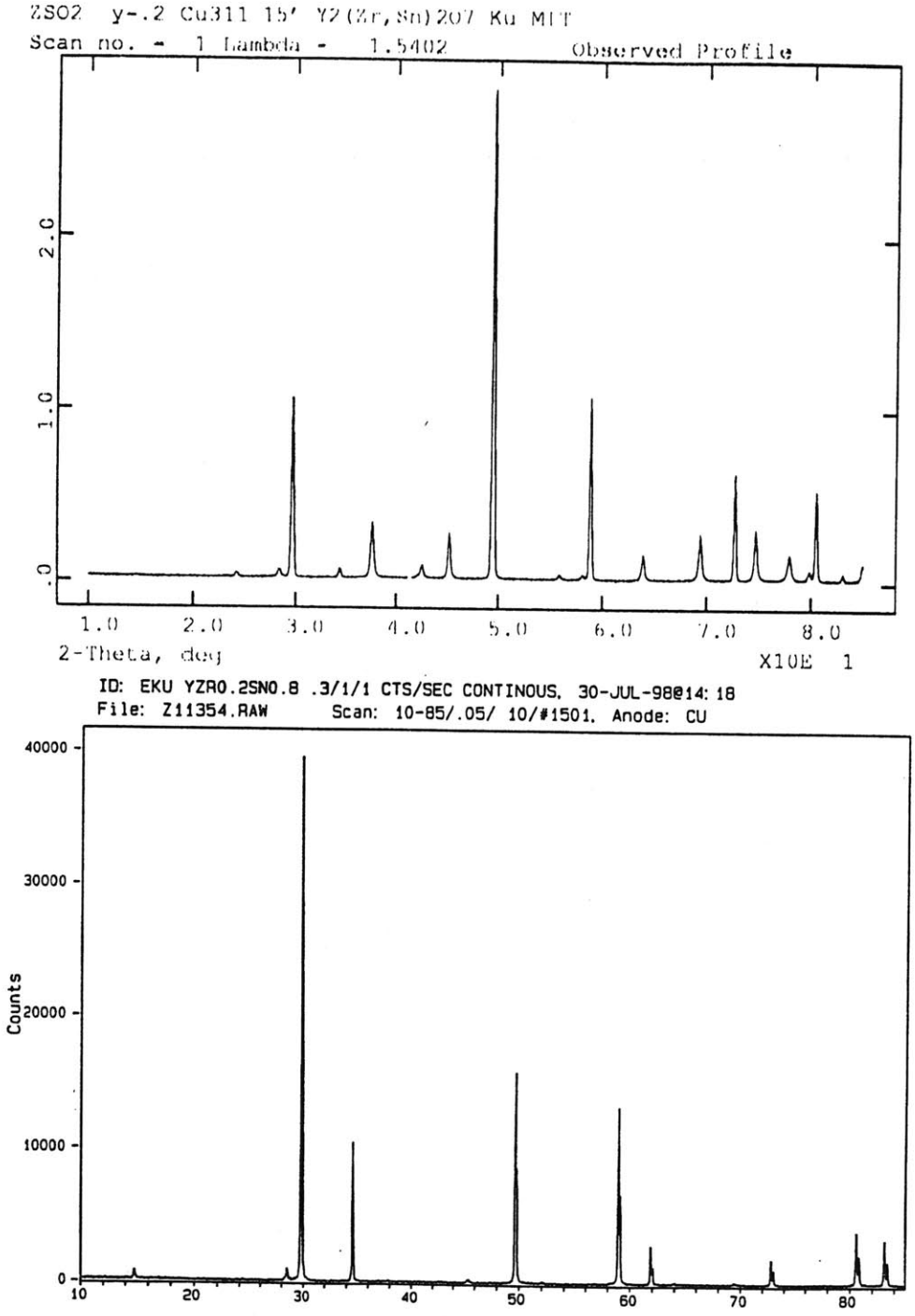

Figure 3.1 *A comparison of the magnitude of the superstructure peaks with those of the substructure as seen in the low angle regions in the* ***(a)*** *neutron diffraction and* ***(b)*** *x-ray diffraction patterns for* $Y_2(Zr_{0.2}Sn_{0.8})_2O_7$. *Note the greater number of peaks visible at higher angles in the neutron pattern.*

radiation used in these experiments were very similar (1.5402 Å and 1.5405 Å respectively), a given reflection in the neutron profile can be found within the same general 2θ region in the other according to Bragg's Law. The inherent differences in the scattering processes of the two types of radiation can be further appreciated from a comparision of the patterns. Since x-rays interact strongly with high-electron count species and are most intense at low angles, the maxima in 3.1(b) can be found at the low angle region and correspond to substructure cation-reflections. On the other hand, in the neutron diffraction pattern, in which scattering is angle-independent, can contain maxima at higher scattering angles than the x-ray pattern and correspond to substructure cation and anion reflections. Thus, at approximately 30°, the (222) reflection which is a fluorite-substructure peak associated with the cations, is the most intense peak found in the entire x-ray pattern, but less intense in the neutron pattern. The (440) fluorite reflection at about $50^{\circ}$is most intense in the neutron pattern since both cations and oxygen ions contribute to the peak. Furthermore, the challenge of analyzing the superlattice peaks can be further appreciated when examining the sheer magnitude of the substructure peaks compared with the superstructure maxima. Specifically, the fluorite (222) reflection as observed in the x-ray pattern exceeds the highest intensity superstructure peak, the (311) reflection at 28°, by three-orders-of-magnitude. The remaining superstructure peaks in the x-ray pattern are not nearly as intense as the (311) reflection and weaken with increasing Zr content.

Figure 3.2(a)-(h) depicts the low angle regions of the observed and calculated neutron ((a)-(d)) and x-ray ((e)-(h)) diffraction patterns for entire solid solution series. The substructure maxima have been excluded in the profiles and superstructure reflections are labeled in the y=0.2 patterns as a reference. The progressive weakening of the superstructure reflections becomes apparent as the Zr content, y, increases, and as the background takes on greater significance (notice should be taken of the change in the scale to which the intensities ae plotted as y increases!). Located at the lower portion of Fig. 3.2.(a)-(h), difference plots

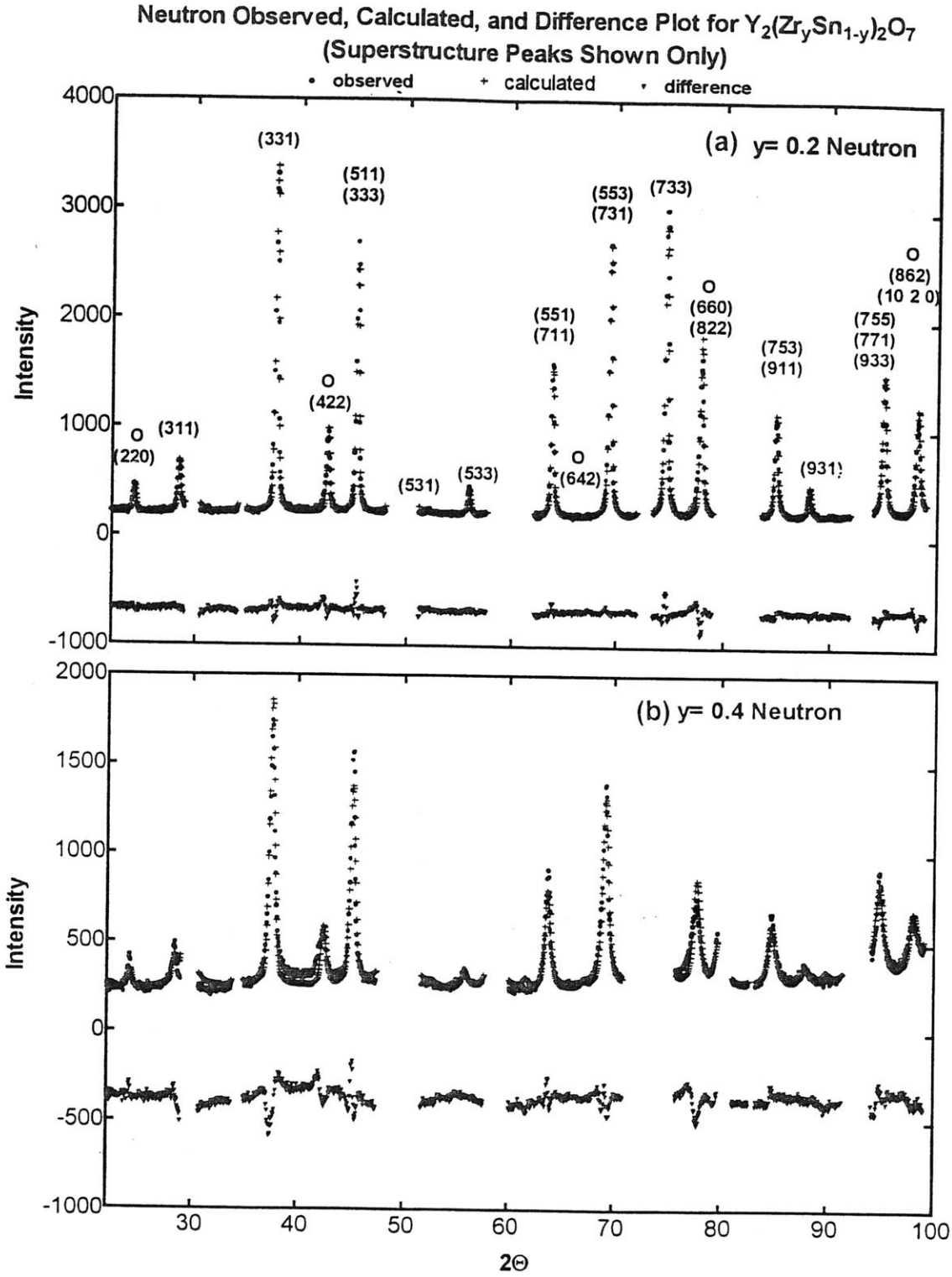

Figure 3.2 (a), (b), (c), (d) *Neutron powder diffraction profiles for y=0.2, y=0.4, y=0.6, and y=0.8 respectively. The difference between the observed and calculated intensity is plotted in the negative y region of the graph. The y=0.2 profile has all the superstructure planes labelled and can serve as a guide. A capital O denotes peaks where only oxygen ions contribute.*

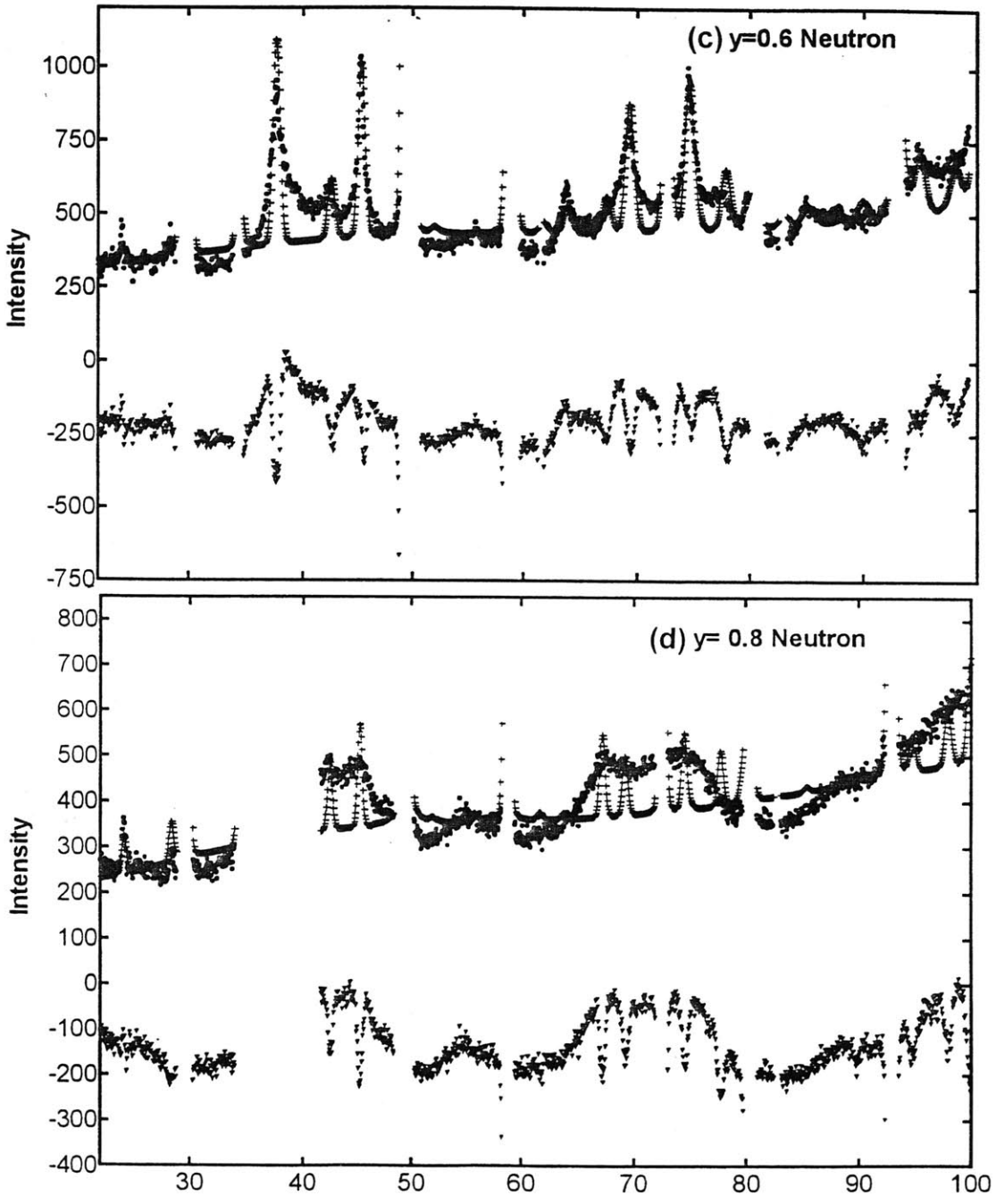
(c) y=0.6 Neutron
Intensity
1000
750
500
250
0
-250
-500
-750
(d) y= 0.8 Neutron
Intensity
800
700
600
500
400
300
200
100
0
-100
-200
-300
-400
30
40
50
60
70
80
90
100

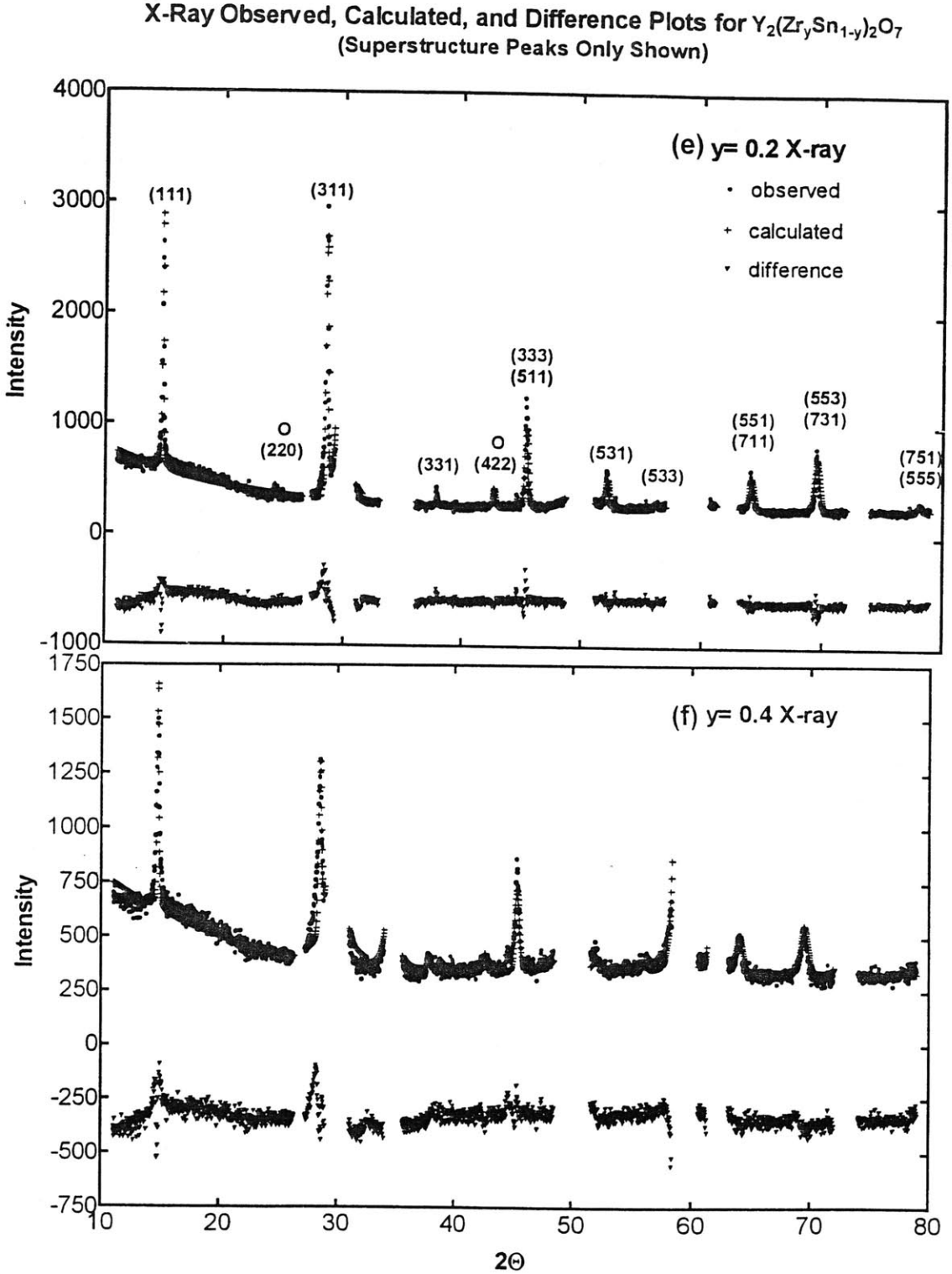

Figure 3.2 (e), (f), (g), (h) *X-ray powder diffraction profiles for y=0.2, y=0.4, y=0.6, and y=0.8 respectively. The difference between the observed and calculated intensity is plotted in the negative y region of the graph. The y=0.2 profile has all the superstructure planes labelled and can serve as a guide. A capital O denotes peaks where only oxygen ions contribute.*

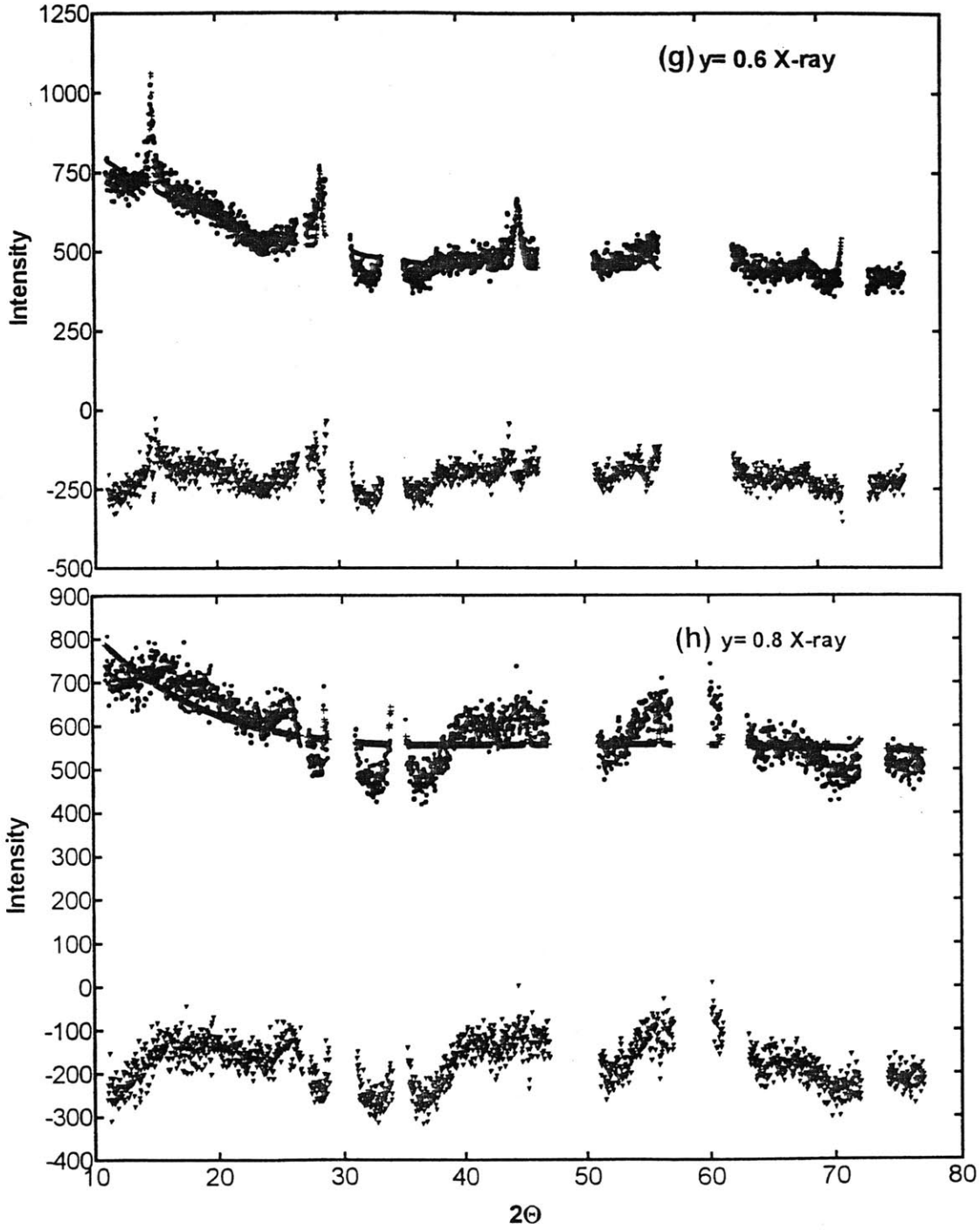
(g) y= 0.6 X-ray
Intensity
1250
1000
750
500
250
0
-250
-500
(h) y= 0.8 X-ray
Intensity
900
800
700
600
500
400
300
200
100
0
-100
-200
-300
-400
10
20
30
40
50
60
70
80
2Θ

between the experimentally observed and calculated values of the pattern are useful indicators of the quality of the Rietveld-analyzed data.

Table 3.1 and 3.2 lists the Rietveld-refined structural parameters for the results of the neutron and x-ray diffraction analyses respectively. Refer to Table 1.1 for definitions of the different residuals. Results of a neutron diffraction analysis of $Y_2Sn_2O_7$ (y=0) by Eberman [4] are also included. The progressive increase in the residuals with Zr content can be attributed to weaker and broader superstructure peaks as well as the growth of a co-existing fluorite-like phase similar to that found in the $Y_2(Zr_yTi_{1-y})_2O_7$ series [1,2,24,29,30]. It seems that standard deviations of refined parameters, and the Bragg residuals rise with increasing disorder. .The fluorite-like phase present in this study's samples has a slightly larger lattice parameter than that of the superstructure, and also has a dramatically different peak-shape. Table 3.3 shows the x-ray refined values obtained when the fluorite peaks to which only the cations contribute (step 1 of the outline procedures in Section 3.1). The differences in lattice constant, peak shape, and significantly-improved residuals are apparent when compared with Table 3.2.

The presence of the co-existing fluorite phase may also account for deviations from a truly linear dependence in lattice parameter with increasing Zr^{4+} substitution of the superstructure, Fig. 3.3. General agreement between the x-ray and neutron results is obtained with the exception at y=0.8 in which the structure approaches complete disorder. An estimate of the amount of fluorite that is present and how it changes with y would be a useful and interesting problem for future work, especially in considering how conductivity relates to structure. Oxygen-ion mobility in the coexisting fluorite phase or antiphase boundaries offers another possible mechanism for conductivity observed in zirconate pyrochlore oxide powders.

Table 3.1. Neutron Derived Lattice Constants, Atomic Coordinates, Site Occupancies and Anisotropic Temperature Factor Coefficients for the $Y_2(Zr_ySn_{1-y})_2O_7$

y=	0	0.2	0.4	0.6	0.8
a (Angstroms)	10.3747(2)	10.3882(1)	10.3962(6)	10.3979(25)	10.4019(21)
A in 16c $\bar{3}$m 0 0 0					
N	0.88(4)	0.97(2)	1.01(3)	0.95(9)	0.92(7)
β 11= β22= β33		0.014(2)	0.010(2)	0.014(5)	0.009(5)
β12=β13=β23		-0.0023(8)	-0.002(1)	-0.004(3)	-0.002(2)
B in 16d $\bar{3}$m 1/2 1/2 1/2					
β 11= β22= β33		0.020(4)	0.012(3)	0.017(6)	0.010(6)
β12=β13=β23		-0.001(1)	-0.003(2)	-0.0016(38)	-0.0006(22)
O(1) in 48f mm x 1/8 1/8					
N	1.00	0.96(2)	0.94(3)	0.89(7)	0.91(5)
x	0.4130(1)	0.4119(4)	0.4100(9)	0.4013(34)	0.383(7)
β11		0.0007(4)	0.0007(12)	0.0097(46)	0.014(7)
β22=β33		0.0015(3)	0.0027(8)	0.0096(31)	0.011(4)
β23		-0.0016(6)	-0.002(1)	-0.011(4)	-0.010(5)
O(2) in 8a $\bar{4}$3m 1/8 1/8 1/8					
N	0.997(9)	0.94(3)	0.89(7)	0.92(21)	1.05(22)
β 11= β22= β33		0.0016(7)	0.004(2)	0.019(11)	0.02(2)
O(3) in 8b $\bar{4}\bar{3}$m 3/8 3/8 3/8					
N	0.003(9)	0.27(5)	0.47(10)	0.74(28)	0.52(27)
β 11= β22= β33		0.21(15)	0.06(4)	0.07(7)	0.03(5)
Rp (%)	7.17	4.75	6.49	8.32	8.40
Rwp (%)	9.20	6.33	8.66	11.07	10.91
Re (%)	8.54	5.24	5.06	4.35	4.78
RB	4.36	3.10	7.24	30.46	57.18
RF		2.77	4.19	15.69	32.66
d		0.5804	0.3024	0.1649	0.164
S		1.2072	1.7122	2.5442	2.2813

Note: Values for y=0 are based on past studies by Eberman[3]

Table 3.2. X-Ray Derived Lattice Constants, Atomic Coordinates, Site Occupancies and Anisotropic Temperature Factor Coefficients for $Y_2(Zr_ySn_{1-y})_2O_7$

y=	0.2	0.4	0.6	0.8
a (Angstroms)	10.3910(9)	10.3971(18)	10.399(5)	10.4126(22)
A in 16c 3m 0 0 0				
N (Occupancy) for Sn4+	0.08(1)	0.16(2)	0.07(2)	0.06(11)
N for Y3+/Zr4+	0.92	0.84	0.93	0.94
β 11= β22= β33	0.008(1)	0.012(1)	0.009(1)	0.005(4)
β12=β13=β23	-0.0007(5)	-0.002(1)	-0.0031(9)	0.00001(86)
B in 16d 3m 1/2 1/2 1/2				
N(Occupancy) for Sn4+	0.72	0.44	0.33	0.14
N for Y3+/Zr4+	0.28	0.56	0.67	0.86
β 11= β22= β33	0.0041(5)	0.063(5)	0.009(1)	0.006(4)
β12=β13=β23	-0.0002(4)	-0.00003(73)	0.0003(10)	0.001(1)
O(1) in 48f mm x 1/8 1/8				
N	0.94(3)	0.89(4)	0.89	0.86(3)
x	0.412(2)	0.410(4)	0.398(45)	0.377(26)
β11	0.007(4)	0.02(1)	0.10(5)	0.01(2)
β22=β33	-0.005(2)	0.003(4)	0.006(8)	0.03(2)
β23	-0.0009(18)	-0.0004(31)	-0.004(8)	-0.02(1)
O(2) in 8a 43m 1/8 1/8 1/8				
N	1.00	1.00	0.920	0.88(23)
β 11= β22= β33	0.001(2)	0.006(4)	0.008(12)	0.05(4)
O(3) in 8b 43m 3/8 3/8 3/8				
N	0.337	0.661	0.740	0.94
β 11= β22= β33	0.25(14)	0.16(6)	0.3(16)	0.04(4)
U	0.05537(4)	0.1507(1)	0.2850(3)	0.00151(3)
X	0.0614(5)	0.0919(8)	0.013(2)	-0.017(2)
Y	-0.007(2)	-0.092(3)	-0.014(8)	0.131(3)
Specimen Displacement Ds	-0.04296414(4)	-0.0470747(2)	-0.011288(1)	-0.040166(5)
Speciment Transparency Ts	-0.0136433(6)	0.006889(3)	-0.00997(2)	-0.01609(1)
Rp (%)	6.75	5.95	5.43	5.61
Rwp (%)	8.56	7.70	7.00	7.26
Re (%)	5.38	4.89	4.43	4.08
RB	17.09	32.39	43.75	64.63
RF	9.60	18.57	21.64	43.31
d	0.8607	0.8224	0.8512	0.6471
S	1.5901	1.5747	1.5800	1.7779

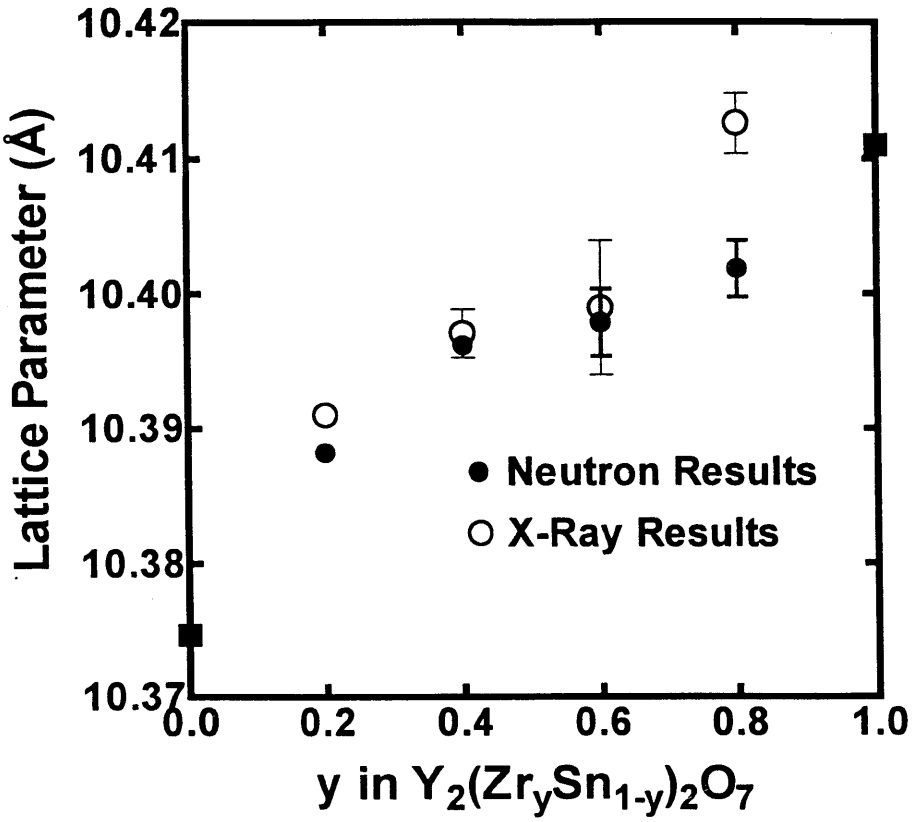

Figure 3.3 *Variation of the lattice constant of* $Y_2(Zr_ySn_{1-y})_2O_7$ *with increasing Zr content from neutron and x-ray analyses. Deviations from linearity in the variation may be a result of the poor resolution of superstructure peaks from the background combined with the co-existing fluorite phase that has a slightly larger lattice constant than the superstructure.*

Table 3.3 X-ray Derived Lattice Constant, Peak-Shape, and Residuals for the Substructure Peaks in which Cations Contribute only

y=	0.2	0.4	0.6	0.8
a (Angstroms)	10.38994(4)	10.39820(4)	10.40627(4)	10.41321(5)
U	0.0007494(6)	-0.0005324(6)	0.0004482(6)	0.0004181(5)
X	0.02308(7)	0.03670(7)	0.3990(7)	0.02061(7)
Y	0.0406(2)	0.0297(2)	0.0304(2)	0.0302(2)
Rp(%)	5.13	4.85	4.63	5.26
Rwp(%)	7.35	6.73	6.32	7.19
Re(%)	3.15	3.06	3.20	2.90
RB(%)	1.04	1.26	1.66	1.42
RF(%)	3.67	3.77	7.17	7.17
d	0.5896	0.6704	0.6722	0.6044
S	2.3354	2.2006	1.9753	2.4809

3.2.2.1 Order and Disorder in the Pyrochlore Structure

The $Y_2(Zr_ySn_{1-y})_2O_7$ series of solid solutions shows striking similarities to the progressive disorder found in the $Y_2(Zr_yTi_{1-y})_2O_7$ series. Fig. 3.4 contrasts the behavior of x-coordinate O(1) of the aforementioned $Y_2(Zr_yTi_{1-y})_2O_7$ and $Y_2(Sn_yTi_{1-y})_2O_7$ systems. While the zirconate series shows a quadratic relationship of the x-coordinate with increasing Zr, the stannate series shows a linear relationship with increasing Sn [1,4]. Fig. 3.5 is a plot of the behavior of the O(1) x-coordinate with change in composition, y, in $Y_2(Zr_ySn_{1-y})_2O_7$ and shows a similar quadratic decrease with Zr^{4+} content as clearly seen in $Y_2(Zr_yTi_{1-y})_2O_7$.

For the $Y_2(Zr_yTi_{1-y})_2O_7$ series, independent disorder rates between the cations and among the three different anions were observed: O(1) and O(3) were engaged in early stages of disorder at y=0.3; mixing between the cation sites begins between y=0.45 and 0.60; and final participation of O(2) occurred at y=0.60 followed by complete disorder in both arrays at y=0.90, Fig. 3.6 [2]. Yeo's [5,43] earlier x-ray analyses of the $Y_2(Zr_ySn_{1-y})_2O_7$ series reveals a similar trend, shown in Fig. 3.7, which shows oxygen occupancies as a function of

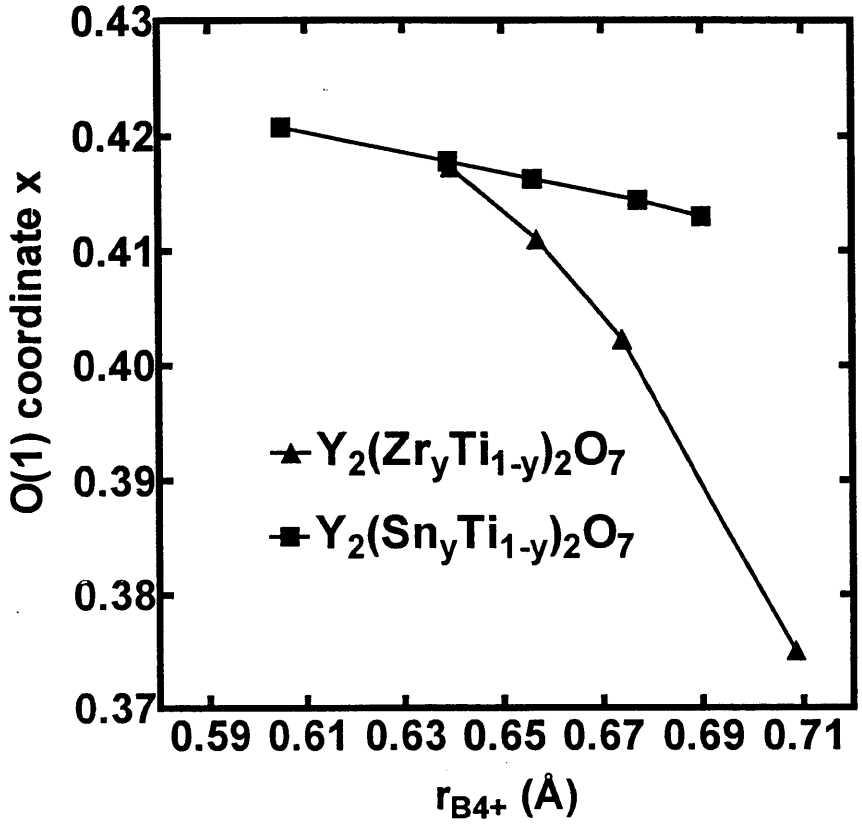

Figure 3.4 *A comparison of the change in the x coordinate for O(1) as a function of the mean radius of the cations nominally occupying the B site for* $Y_2(Zr_yTi_{1-y})_2O_7$, *a system displaying disorder in the anion and cation arrays (quadratically decreasing x), and for* $Y_2(Sn_yTi_{1-y})_2O_7$, *an essentially ordered system at all compositions (linearly decreasing x) [3].*

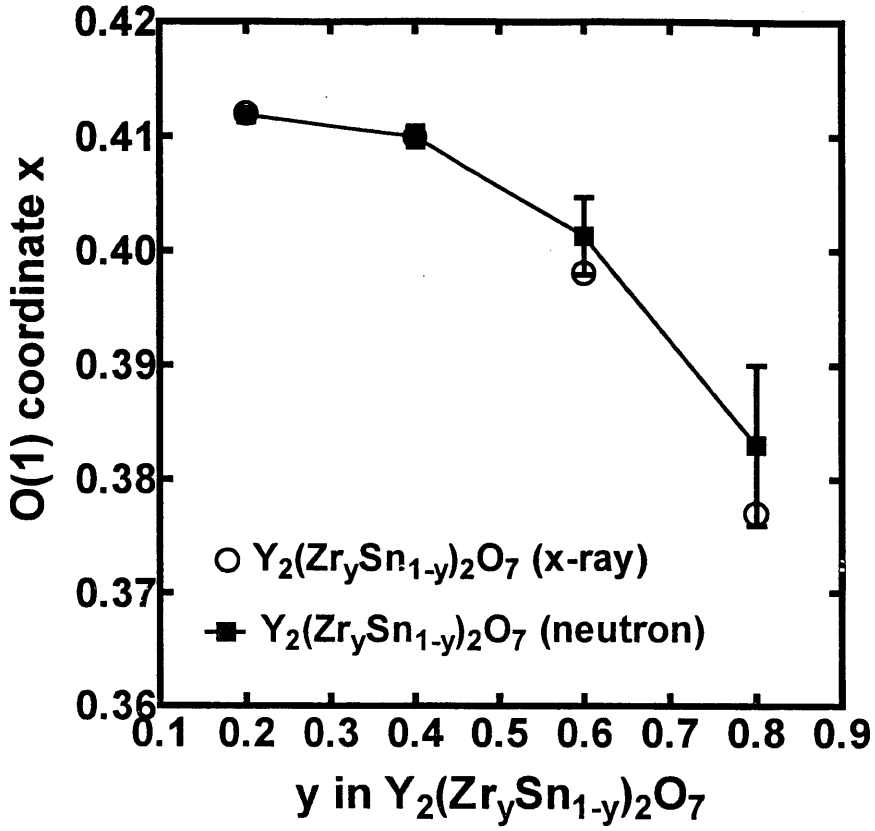

Figure 3.5 *Quadratically-decreasing O(1) x-coordinate with increasing amounts of Zr in* $Y_2(Zr_ySn_{1-y})_2O_7$. *Neutron and x-ray analyses show good agreement.*

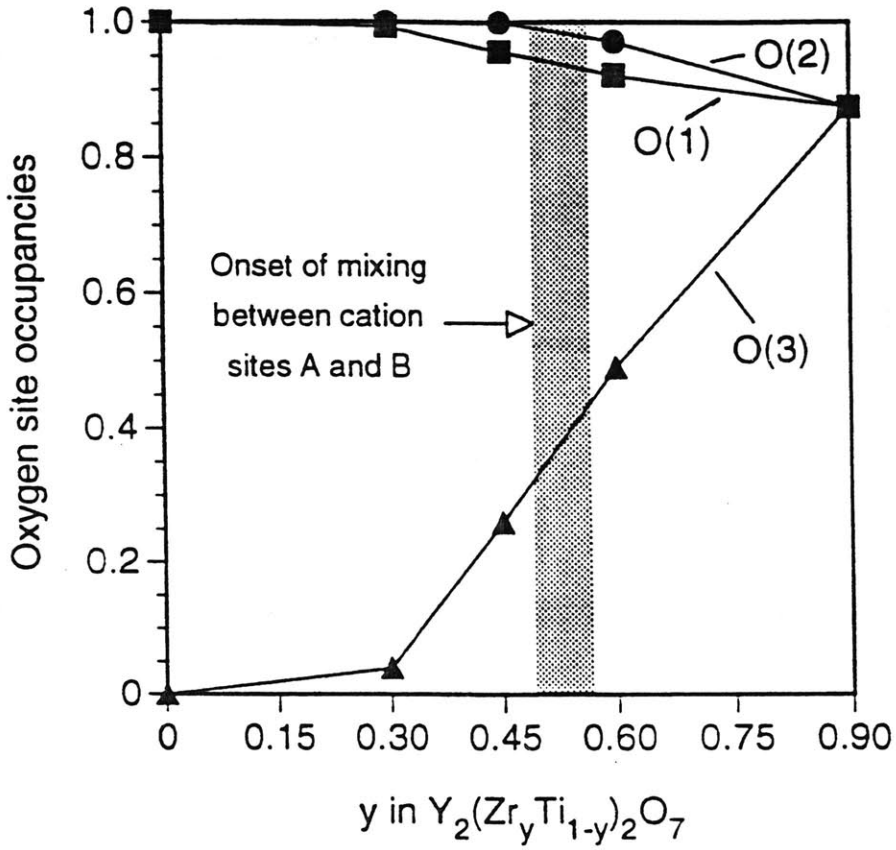

Figure 3.6 *Neutron diffraction analyses by Heremans [1,2] of* $Y_2(Zr_yTi_{1-y})_2O_7$ *show the change in anion occupancies as a function of Zr content y. O(2) is involved in disorder midway through the solid solution series after mixing of the cation occupancies.*

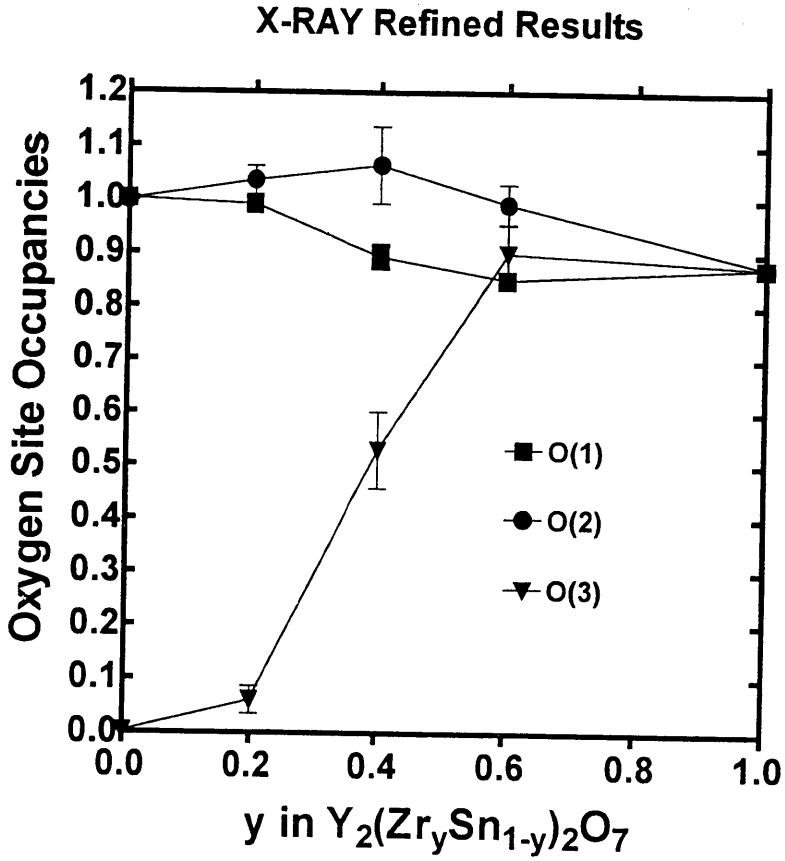

Figure 3.7 *Results of preliminary x-ray studies by Yeo [5,43] showing the change in the occupancies of the anion sites as a function of increasing Zr content, y, in* $Y_2(Zr_ySn_{1-y})_2O_7$. *The y=0 value is taken from neutron diffraction studies by Eberman [3]. Like* $Y_2(Zr_yTi_{1-y})_2O_7$ *[2], the oxygen ions in* $Y_2(Zr_ySn_{1-y})_2O_7$ *display independent disordering rates.*

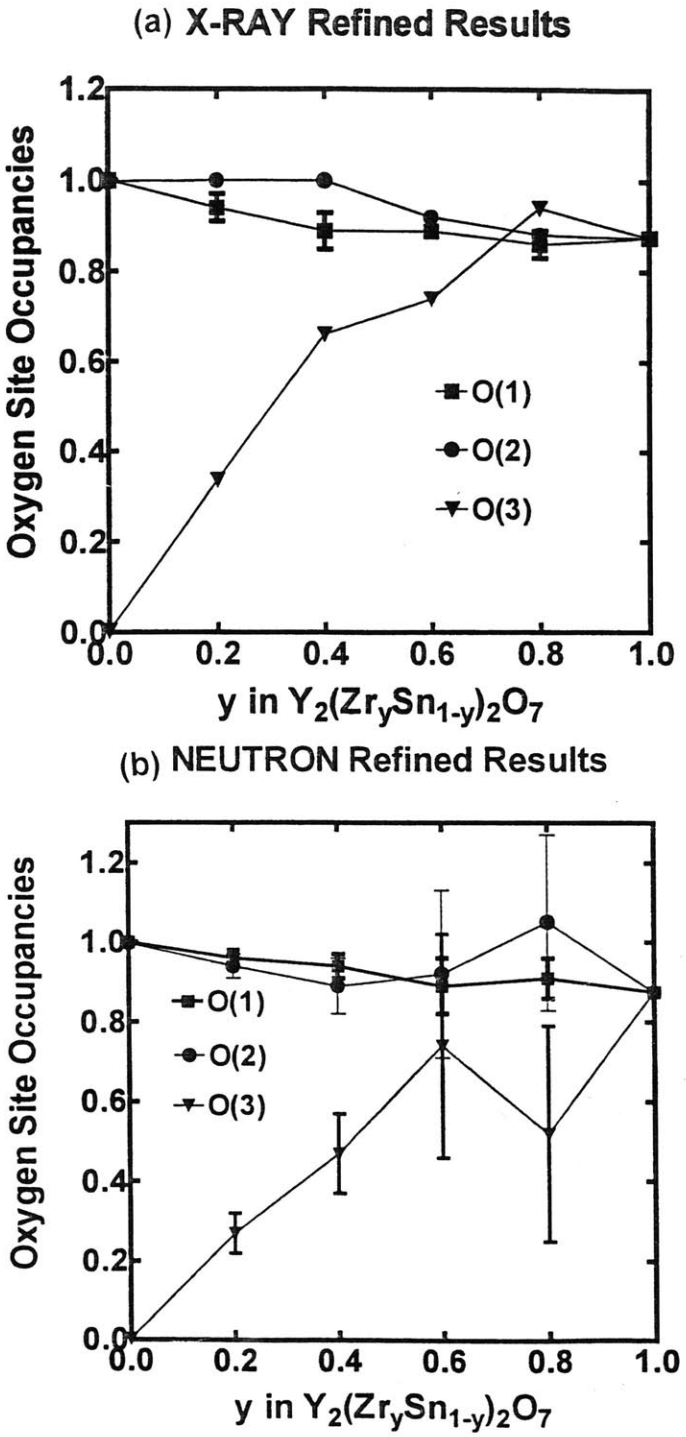

Figure 3.8 ***(a)*** *X-ray diffraction data of this study showing the change in occupancies of the oxygen ion array as a function of increasing Zr content, y, in* $Y_2(Zr_ySn_{1-y})_2O_7$. *General agreement is also seen with Yeo's results, but anion disorder occurs almost immediately upon addition of Zr as seen in the linear increase of the O(3) occupancy.* ***(b)*** *Neutron data, a more sensitive measure of oxygen occupancies, showing the change in the occupancies of the anion sites as a function of Zr content in* $Y_2(Zr_ySn_{1-y})_2O_7$. *Disorder in both the cation and anion arrays begin as almost immediately upon increase of y. High standard deviations of the oxygen occupancies at y=0.8 is due to the increased presence of a co-exising fluorite-like phase coupled with weaker superstructure intensities.*

increasing Zr content. The x-ray results of this study, Fig. 3.8(a), closely resemble Yeo's work, but suggests a immediate disorder of the anion array as noted by the linear increase of the O(3) occupancy from y=0. Oxygen ion occupancies for y=0.6 in the x-ray analyses were fixed at the values obtained from the neutron refinement since nonsensical values were obtained when these parameters were allowed to vary

The neutron data, which provide a more sensitive measure of oxygen occupancies, also suggests disorder in O(1) and O(3) and slight levels within O(2) immediately upon addition of Zr as seems to increase linearly with y, Fig. 3.8(b). At y=0.2 the average B^{4+} site radius is 0.696 Å corresponding to $(Zr_{0.8}Ti_{0.2})$ which would have already showed levels of disorder in both the cation and anion arrays in the zirconium-titanium pyrochlores. Figure 3.9 is a comparison of the O(1) x-coordinate as a function of average ionic radius of site B of the three solid solution series, $Y_2(Zr_yTi_{1-y})_2O_7$, $Y_2(Sn_yTi_{1-y})_2O_7$, and $Y_2(Zr_ySn_{1-y})_2O_7$. Previous studies of $Y_2Sn_2O_7$ by Eberman [4] indicated levels of cation disorder but no anion disorder. Clearly, results of both the neutron and x-ray analyses in the present study agree that the anion array is not completely disordered (when all the anion site occupancies of the defect fluorite state would be $^7/_8$) for Zr substitution extending to y=0.6. In fact, neutron diffraction data of y=0.8 still showed signs of very weak maxima for those superstructure peaks occurring at low angles as seen in Fig. 3.2(d). The extreme weakening of intensities of superstructure peaks in the neutron diffraction data, and the virtually non-existent peaks buried in the background for the x-ray data at y=0.8 made accurate structural analyses difficult as seen in the high standard deviations of the oxygen occupancies in Tables 3.1, 3.2 and Fig. 3.9. Overall, the Zr present in the $Y_2(Zr_ySn_{1-y})_2O_7$ series appears to override the tendency of Sn to maintain an ordered structure. This suggests that Zr^{4+}, as a consequence of its larger size, has greater ability to enter the eight-coordinated A site than the Sn^{4+}, which has Sn-O bonds possessing significant covalent character.

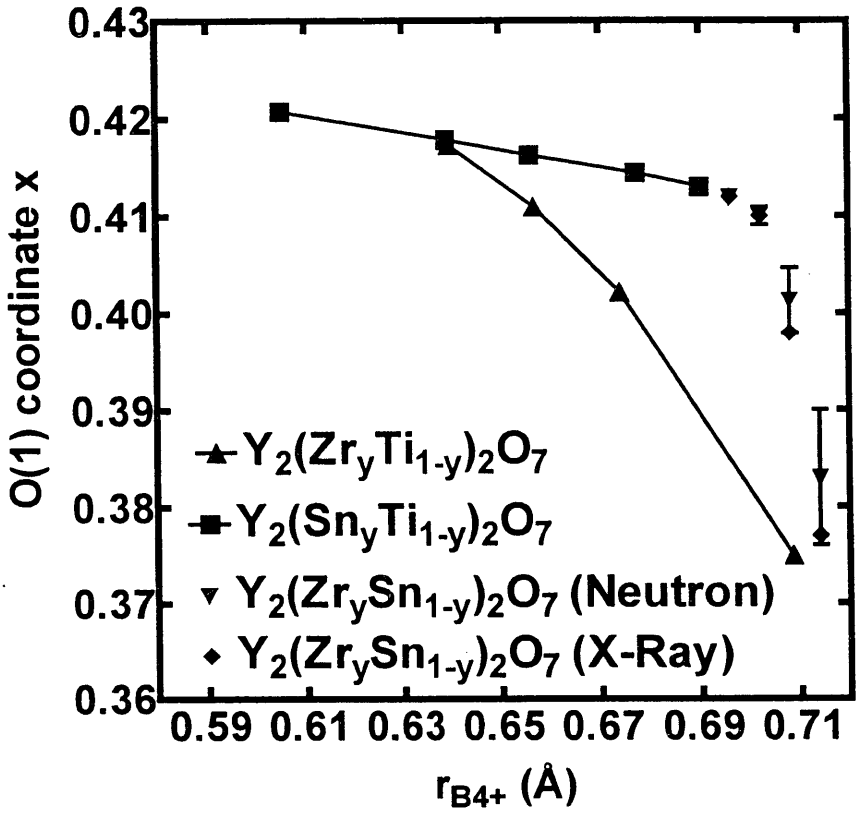

Figure 3.9 *Comparison of the O(1) x-coordinate as a function of average ionic radius of the B site in three solid solution series,* $Y_2(Zr_yTi_{1-y})_2O_7$, $Y_2(Sn_yTi_{1-y})_2O_7$, *and* $Y_2(Zr_ySn_{1-y})_2O_7$.

3.2.2.2 Cation Distribution

The effective scattering powers of the A and B cation sites, as reported in Tables 3.1 and 3.2, were employed in the equations outlined in Section 3.1 to calculate the distributions of Sn^{4+}, Zr^{4+} and Y^{3+} cations. The results are listed in Table 3.3. Table 3.5 shows the occupancies in terms of relative percent of the total stoichiometric amount of each cation in the two sites.

Table 3.4 Cation Distribution from Combined X-ray and Neutron Analyses

y	Sn4+ in A	Sn4+ in B	Zr4+ in A	Zr4+ in B	Y3+ in A	Y3+ in B
0.2	0.08(1)	0.7165	0.2181	-0.0181	0.6984	0.3017
0.4	0.16(2)	0.4441	-0.4851	0.8851	1.3292	-0.3292
0.6	0.07(2)	0.3317	0.5243	0.0758	0.4075	0.5925
0.8	0.06(11)	0.1380	0.9000	-0.1000	0.0381	0.9619

Table 3.5 Relative Percent of Total Stoichiometric Amount of Each Cation Distributed in Sites A and B

y	% Sn in A	%Sn in B	%Zr in A	%Zr in B	%Y in A	%Y in B
0.2	10.44	89.56	109.07	-9.07	69.84	30.16
0.4	25.98	74.02	-121.27	221.27	132.92	-32.92
0.6	17.07	82.93	87.37	12.63	40.75	59.25
0.8	30.98	69.02	112.50	-12.50	3.81	96.19

Results of the cation distributions show both surprising and expected trends. A more or less constant amount of Sn^{4+} occupies the A site, averaging approximately 20% (with standard deviations considered) of the total amount of Sn^{4+} present in the solid solution. This result is consistent with the results of Eberman[3] who found cation disorder in $Y_2Sn_2O_7$. In fact, he found the Y^{3+} A site occupancy to be only 0.88 ± 0.04 which shows general agreement with this study. The second trend is that Zr^{4+}, as predicted, has an increasing tendency with y to enter the A site; however, a surprising exception to this prediction occurs at y=0.4. At this composition, the results seem to indicate that all the Zr^{4+} remains in the B site based on the "negative" occupancies. However, upon further analysis of the calculations, it became clear

that the necessity of lumping the Zr^{4+} and Y^{3+} together in the x-ray analysis (because of their nearly identical scattering factors) no longer permits computation of partitioning of the three species from the results of the neutron analysis because the neutron data at this composition shows very little contrast in scattering between the A and B sites. More specifically, any combination of values that were substituted for the occupancy of the Sn^{4+} always resulted in a positive and negative occupancy in the respective B and A site for Zr^{4+}; and a positive and negative occupancy in the respective A and B site for Y^{3+}. Thus, we are left with a two cation one site problem here! More than likely, equal amounts of Zr^{4+} and Y^{3+} are found in both sites, leading to indistinguishable scattering lengths (i.e occupancies of 0.2 in the A and B sites for Zr^{4+}, and 0.5 in both sites for Y^{3+}). The distribution of the Zr^{4+} and Y^{3+} occupancies cannot be determined based on the x-ray data and model for analysis. Another linearly-independent diffraction experiment is needed for increased precision.

Another complication in determining the cation distribution in this solid solution series, $Y_2(Zr_ySn_{1-y})_2O_7$, is the presence of the fluorite-like phase. Examination of the amount of fluorite phase present in the powders would better quantify the degree of uncertainty in the values listed in Table 3.4 especially if the lattice constant of this fully-disordered phase indicates a composition that is different from that of the pyrochlore phase. Furthermore, particular cations, like Zr, may have a tendency toward antiphase boundaries. Thus, the amount of Zr available for the pyrochlore regions would be decreased. The same is true of the Y or Sn which may be present in the co-existing fluorite phase. Zaghete [25] used the Rietveld method to perform quantitative analysis of the evolution of the tetragonal and rhombohedral phases of lead zirconate titanate prepared by the Pechini method. The relative amounts of these phases were contingent on composition and calcination temperature. By studying three varying Zr:Ti ratios of 49:51, 53:47, and 57:43, they concluded that the zirconium ion diffused toward titanium-rich regions thereby increasing the amount of tetragonal phase for

compositions with zirconium less than 53% and decreasing the tetragonal phase for compositions with zirconium greater than 53%. A similar treatment of the solid solution series of this study could provide further insight into the cation distribution in the pyrochlore structure.

4. Conclusions

The present structural analyses of the solid solution series, $Y_2(Zr_ySn_{1-y})_2O_7$, provide insight into the marked contrasts between the highly ordered Ti stannate series, $Y_2(Sn_yTi_{1-y})_2O_7$ and the Ti zirconates, $Y_2(Zr_yTi_{1-y})_2O_7$. Rietveld analyses of neutron and x-ray data of the $Y_2(Zr_ySn_{1-y})_2O_7$ system shows marked similarities with the $Y_2(Zr_yTi_{1-y})_2O_7$ solid solution series. Like the Ti zirconates, the O(1) coordinate x decreased quadratically with increased Zr content, y, a hallmark of the creation of disorder in the cation and anion arrays. Results from both the x-ray and neutron analyses suggest almost immediate cation and anion disorder upon addition of Zr. Furthermore, complete disorder of the pyrochlore structure to the defect fluorite phase seems to occur slightly beyond y=0.8.

Combined analyses of x-ray and neutron diffraction data was used in an attempt to determine distribution of three cations in two cystallographically independent sites. Separating superstructure peaks from the background became increasingly difficult with increasing Zr content,y, because of rapidly-increasing disorder and the general lack of contrast between the three cation species for both x-rays and neutrons. Poor resolution of the superstructure peaks also account for rising residuals and standard deviations with increase in y. The results show an essentially constant amount of Sn^{4+} remains in the A site for the highly-ordered, low Zr solid solutions. This corresponds to approximately the same level of cation disorder found in

$Y_2Sn_2O_7$ found by Eberman [3]. Furthermore, Zr^{4+} readily enters the A site beginning as early as y=0.2 . The cation partitioning of the Zr^{4+} and Y^{3+} for y=0.4 can be more precisely solved with another independent diffraction experiment.

The presence of a co-existing fluorite-type phase presented additional challenges in examination of the $Y_2(Zr_ySn_{1-y})_2O_7$ series. The fluorite phase seemed to have a slightly larger lattice constant than that refined for the superstructure which could be indicative of a composition different from that of the pyrochlore phase. Departure from the nominal composition of the latter could explain deviations from linear dependence of the lattice constant on increasing Zr content. Moreover, the cation distribution determined for the superstructure may be offset by the cations that may have a tendency toward antiphase boundaries or the fluorite-like phase. Nonetheless, preliminary analysis of combined neutron and x-ray data seems to reveal more similarities of the present $Y_2(Zr_ySn_{1-y})_2O_7$ compositions with the $Y_2(Zr_yTi_{1-y})_2O_7$ series than with the order that persists in $Y_2(Sn_yTi_{1-y})_2O_7$. Overall, the examination of disorder and cation distributions in this study suggests an ability of Zr to more readily enter the eight-coordinated A site than is the case for the covalently-bonded Sn. The fact that the progress of cation and anion disorder with increasing Zr content has been shown to be quite similar to that in the $Y_2(Zr_yTi_{1-y})_2O_7$ system, previously show to be an excellent fast-ion conductor, allows one to predict that the newly-synthesized $Y_2(Zr_ySn_{1-y})_2O_7$ compositions will prove to be equally-outstanding conductors.

5. Future Work

A number of interesting problems and areas for further research are generated from this investigation. As found by previous studies, antiphase boundaries in pyrochlore solid solutions were common in samples using a modified Pechini method or a citrate metal precursor technique [1,2,24,29,30]. An interesting question is if another synthesis method would give the same structural analysis results. Eberman [3] attempted to address this question by synthesizing compositions of pyrochlore via solid state reaction, but concluded that the samples were actually different in nominal composition. Thus, the question of whether antiphase boundaries are common to all polycrystalline pyrochlore compounds or simply a result of the synthesis route remains to be determined. Quantifying the amount of fluorite present in the solid solution powders would be useful in determining more accurate lattice parameters and the cation distribution of the superstructure.

Yu[5] has studied the ionic conductivity measurements of $Gd_2(Zr_ySn_{1-y})_2O_7$. It would be interesting to see how the conductivity of $Y_2(Zr_ySn_{1-y})_2O_7$ compares with the gadolinium counterpart as the structural insights of disorder in this study predict that the newly-synthesized yttrium zirconium stannates should display high oxygen ion conductivities comparable to $Y_2(Zr_yTi_{1-y})_2O_7$.

While this is the first study to employ two radiation to analyze the cation distribution in a pyrochlore compound, other pyrochlore compounds that have greater differences in scattering lengths may be more amenable to analysis with increased accuracy and precision. The use of synchrotron x-ray radiation with wavelengths close to the absorption edge of one or more of the cations can also be used to enhance superstructure intensities, as the effective scattering power of a cation may thereby be shifted by as many as a dozen electrons.

Substituting all three cations Zr^{4+} , Sn^{4+}, and Ti^{4+} in the B site of our pseudo-ternary system, $Y_2Ti_2O_7$ -$Y_2Sn_2O_7$ -$Y_2Zr_2O_7$, would add further insight into this system and perhaps reveal conductivities that are further enhanced. Moreover, as mentioned by Eberman [3], an A-site substitution series would also provide great insight into factors that control ordering in the pyrochlore structure.

References:

1. C. Heremans, B. J. Wuensch, J. K Stalick, and E. Prince, "Fast-Ion Conducting $Y_2(Zr_yTi_{1-y})_2O_7$ Pyrochlores: Neutron Rietveld Analysis of Disorder Induced by Zr Substitution," Journal of Solid State Chemistry **117**, 108-121 (1995).

2. C. Heremans, Fast-Ion Conductors: Single Crystal Growth of Copper and Silver Halides and Structural Determination of $Y_2(Zr_yTi_{1-y})_2O_7$ Pyrochlores, Ph.D. Thesis, MIT, Cambridge (1993).

3. K.W. Eberman, Crystallographic Origins of Fast-Ion Conduction in Pyrochlore, Ph.D. Thesis, MIT, Cambridge (1998).

4. E. M. E. Yeo, Synthesis and Rietveld X-Ray Analysis of $Y_2(Zr_ySn_{1-y})_2O_7$ Pyrochlore Powders: Disordering with Zr Substitution, S.B. Thesis, MIT, Cambridge (1998).

5. T.H. Yu, Electrical Properties and Structural Disorder in Stannate Pyrochlores, Ph.D. Thesis, MIT, Cambridge (1996).

6. P. K. Moon, Electrical Conductivity and Structural Disorder in $Gd_2Ti_2O_7$-$Gd_2Zr_2O_7$ and $Y_2Ti_2O_7$-$Y_2Zr_2O_7$ Solid Solutions, Ph.D. Thesis, MIT, Cambridge (1988).

7. J. E. Post and D. L Bish, "Rietveld Refinement of Crystal Structures Using Powder X-Ray Diffraction Data," pp. 277-308 in Modern Powder Diffraction, Reviews in Mineralogy, Vol. 20. Edited by D.L. Bish and J. E. Post. The Mineralogical Society of America, Washington, D. C., 1989.

8. R. B Von Dreele, "Neutron Powder Diffraction," pp. 333-369 in Modern Powder Diffraction, Reviews in Mineralogy, Vol. 20. Edited by D.L. Bish and J. E. Post. The Mineralogical Society of America, Washington, D. C., 1989.

9. R. D. Shannon, "Revised Effective Ionic Radii and Systemmatic Studies of Interatomic Distances in Halides and Chalogenides," Acta Crystallographica **A32**, 751-767 (1976).

10. C. Petit, J. L. Rehspringer, A. Kaddouri, S. Libs, P. Poix, and A. Kiennemann, "Oxidative Coupling of Methane by Pyrochlore Oxide $A_2B_2O_7$ (A=Rare Earth, B= Ti, Zr, Sn). Relation Between C_2 Selectivity and B-O Bond Energy," Catalysis Today **13** 409-416 (1992).

11. P. A. Lessing, "Mixed-Cation Oxide Powders via Polymeric Precursors," Am. Ceram. Soc. Bull., **68** [5] 1002-1007 (1989).

12. L. W. Tai and P. A. Lessing, "Modified Resin-Intermediate Processing of Perovskite Powders: Part I. Optimization of Polymeric Precursors," J. Mater. Res., 7 [2] 502-510 (1992).

13. L. W. Tai and P. A. Lessing, "Modified Resin-Intermediate Processing of Perovskite Powders: Part II. Processing for Fine, Nonagglomerated Sr-doped Lanthanum Chromite Powders," J. Mater. Res., **7** [2] 502-510 (1992).

14. P. Singh, S. R. Sainkar, M. V. Kuber, V. G. Gunjikar, R. F. Shinde and S.K. Date, "La-Stabilized Zirconia: Synthesis and Characterization," Mater. Lett. **9** [2,3] 65-70 (1990).

15. S.C. Zhang, G. L. Messing, W. Huebner, and M. M. Coleman, "Synthesis of $YBa_2Cu_3O_{7-x}$ Fibers from an Organic Acid Solution," J. Mater. Res. **5** [9] 1806-1812 (1990).

16. J. H. Choy and Y. S. Han, "Citrate route to the Preparation of Nanometer Size (Pb, La)(Zr, Ti)O_3 Oxide," Mater. Lett. **32** 209-215 (1997).

17. J. H. Choy and Y. S. Han, "Citrate route to the Piezoelectric Pb(Zr, Ti)O_3 Oxide," J. Mater. Chem., **7** [9] 1815-1820 (1997).

18. N. G. Eror and H. U. Anderson, "Polymeric Precursor Synthesis of Ceramic Materials;" pp. 571-77 in Better Ceramics Through Chemistry II, Materials Research Society Symposium Proceedings, Vol. 73. Edited by C. J. Brinker, D. E. Clark, and D. R. Ulrich. Materials Research Society, Pittsburgh, PA, 1986.

19. H. U. Anderson, M. J. Pennell, and J. P. Guha, "Polymeric Synthesis of Lead Magnesium Niobate Powders;" pp. 91-98 in Advances in Ceramics, Vol. 21, Ceramic Powder Science. Edited by G. L. Messing, K. S. Mazdiyasni, J. W. McCauley, and R. A. Haber. American Ceramic Society, Westerville, OH, 1987.

20. M. Kakihana, M. M. Milanova, M. Arima, T. Okubo, M. Yashima, and M. Yoshimura, "Polymerized Complex Route to Synthesis of Pure $Y_2Ti_2O_7$ at 750 °C Using Yttrium-Titanium Mixed-Metal Citric Acid Complex," J. Am. Ceram. Soc **79** [6] 1673-76 (1996).

21. M. M. Milanova, M. Kakihana, M. Arima, M. Yashima, and M. Yoshimura, "A Simple Solution Route to the Synthesis of Pure $La_2Ti_2O_7$ and $Nd_2Ti_2O_7$ at 700-800°C by Polymerized Complex Method," J. of Alloys and Compounds **242** 6-10 (1996).

22. T. Okubo and M. Kakihana, "Low Temperature Synthesis of Y_3NbO_7 by Polymerizable Complex Method: Utilization of a Methanol-Citric Acid Solution of $NbCl_5$ as a Novel Niobium Precursor," J. of Alloys and Compounds **256** 151-154 (1997).

23. M. Liu and D. Wang, "Preparation of $La_{1-z}Sr_zCo_{1-y}Fe_yO_{3-x}$ Thin Films, Membranes, and Coating on Dense Porous Substrates," J. Mater. Res. **10** [12] 3210-3221 (1995).

24. E. R. Leite, M. A. L. Nobre, M. Cerqueira, E. Longo and J. A. Varela, "Particle Growth during Calcination of Polycation Oxides Synthesized by the Polymeric Precursors Method," J. Am. Ceram. Soc. **80** [10] 2649-57 (1997).

25. M. A. Zaghete, C. O. P. Santos, J. A. Varela, E. Longo, and Y. P. Mascarenhas, "Phase Characterization of Lead Zirconate Titanate Obtained from Organic Solutions of Citrates," J. Am. Ceram. Soc. **75** [8] 2088-93 (1992).

26. W. J. Lee and T. T. Fang, "The Effect of the Molar Ratio of Cations and Citric Acid on the Synthesis of Barium Ferrite Using a Citrate Process," J. Mater. Sci. **30** 4349-4354 (1995).

27. P. G. Harrison, *Chemistry of Tin*, Chapman and Hall, New York, New York (1989) pgs. 119, 135-136.

28. M.P. Pechini, "Method of Preparing Lead and Alkaline Earth Titanites and Niobates and Coating Method Using the Same to Form a Capacitor," U.S. Patent No. 3,330,697. July 11, 1967.

29. M.P. van Dijk, F.C. Mijlhoff, and A.J. Burggraaf, "Pyrochlore Microdomain Formation in Fluorite Oxides," Journal of Solid State Chemistry **62**, 377-385 (1986).

30. M. P. van Dijk, A.J. Burggraaf, A. N. Cormack, C. R. A Catlow "Defect Structures and Migration Mechanisms in Oxide Pyrochlores," Solid State Ionics 17, 159-167 (1985).

31. A. Williams, G.H. Kwei, R.B. Von Dreele, A. C. Larson, I. D. Raistrick and D. L. Bish, "Joint X-ray and Neutron Refinement of the Structure of Superconducting $YBa_2Cu_3O_7$: Precision structure, Anisotropic Thermal Parameters, Strain, and Cation Disorder," Physical Review B Condensed Matter Ser. 3 **37** [10], 7960-7962 (1988).

32. A. Williams, G.H Kwei, A.T. Ortiz, M. Karnowski, and W. K Warburton, "Combined Neutron and X-ray Powder Diffraction Study of $Fe_{0.05}Co_{0.48}V_{0.02}$," Journal of Material Research **5** [6], 1197-1200 (1990).

33, T. Sakurai, T. Yamashita, J. O Willis, H. Yamauchi, S. Tanaka, and G. H. Kwei, "Combined X-ray and Neutron Powder Diffraction Study of the Structure of $La_{1.8}Sr_{0.2}CaCu_2O_6$: Cation Ordering and Oxygen Stoichiometry," Physica C **174**,187-194 (1991) .

34. K. A. Kubat-Martin, G. H. Kwei, A.C. Lawson, and D.E. Peterson, "Combined X-ray and Neutron Powder Diffraction Study of the Structure of $Ba_4CaCu_3O_x$: Oxtygen Stoichiometry and Cation Order," Journal of Solid State Chemistry **100**, 130-135 (1992).

35. G. H. Kwei, R. B. Von Dreele, A. Williams, J. A. Goldstone, A. C. Lawson II, and W.K. Warburton, " Structure and Valence from Complementary Anolamous X-ray and Neutron Powder Diffraction," Journal of Molecular Structure **223**, 383-406 (1990).

36. J. K. Warner, A. K. Cheetham, and D.E. Cox, "Determination of Cation Distribution in $NiFe_2(PO_4)_2$ using Resonant X-ray and Neutron Powder Diffraction," Journal of Applied Crystallography **28**, 494-502 (1995).

37. A. K Cheetham and A. P. Wilkinson, "Synchrotron X-ray and Neutron Diffraction Studies in Solid-State Chemistry," Angewandte Chemie International Edition in English **31** [12], 1557-1570 (1992).

38. J. L. Finney, "The Complementary Use of X-ray and Neutron Diffraction in the Study of Crystals," Acta Crystallograhica **B51**, 447-467 (1995).

39. F. Izumi, "Rietveld Analysis Programs RIETAN and PREMOS and Special Applications," in *The Rietveld Method*, edited by R.A. Young , Oxford University Press, Oxford, 236-253 (1993).

40. G.H. Kwei, R. B. Von Dreele, S.-W. Cheong, Z. Fisk, J. D. Thompson, Phys. Rev. Sect. B **41**, 1889-1893 (1990).

41. M. A. Subramanian, G. Aravamudan, and G. V. Subba Rao, "Pyrochlore Oxides: A Review," Progress in Solid State Chemistry **15**, 125-143 (1983).

42. B.J. Wuensch and K.W. Eberman, to be published.

43. E.M. Ku, E.M. Yeo, and B.J. Wuensch, to be published in the Solid-State Chemistry of Inorganic Materials II, edited by E.M. Carron III, H-C. zur Loye, S. M. Kauzlarich, A. W. Sleight, 547-L8, Materials Research Society Symposium Proceedings (1998).

44. S.M. Haile, B. J. Wuensch, and E. Prince, "Neutron Rietveld Analysis of Anion and Cation Disorder in the Fast-Ion Conducting Pyrochlore System $Y_2(Zr_xTi_{1-x})_2O_7$," Materials Research Society Symposium Proceedings **166**, 81-86 (1990).

45. B. J. Kennedy, B. A. Hunter, and C. J. Howard, "Structure and Bonding Trends in Tin Pyrochlore Oxides," Journal of Solid State Chemistry **130**, 58-65 (1997).

46. F. Brisse and O. Knop, "Pyrochlores. III. X-ray, Neutron, Infrared, and Dielectric Studies of $A_2Sn_2O_7$ Stannates," Canadian Journal of Chemistry **46**, 859-873 (1967).

47. R.B. Von Dreele, "Combined X-ray and Neutron Rietveld Refinement," in *The Rietveld Method*, edited by R.A. Young , Oxford University Press, Oxford, 227-235 (1993).

48. L.V. Azaroff, M. J. Buerger, in The Powder Method in X-ray Crystallography, McGraw-Hill Book Company, Inc, New York, 1958.

49. H. L. Monaco, "Experimental Methods in X-ray Crystallography," in Fundamentals of Crystallography, edited by C. Giacovazzo, International Union of Crystallography, Oxford University Press, Oxford, pp.287 (1994).

50. R. A. Young, "Introduction to the Rietveld Method," in *The Rietveld Method*, edited by R. A. Young, International Union of Crystallography, Oxford University Press, Oxford, 1-37 (1993).

51. E.N. Maslen, A. G. Fox, M.A. O'Keefe, "Intensity of Diffracted Intensities,"in International Tables for Crystallography, Vol. C: Mathematical, Physical, and Chemical Tables, edited by A.J.C. Wilson, International Union of Crystallography, Kluwer Academic Publishers, Norwell, MA, pp. 476-511, Table 6.1.1.3 (1995).

52. F.Izumi, A Rietveld-Refinement Program Rietan-94 for Angle-Dispersive X-Ray and Neutron Powder Diffraction, National Institute for Research in Inorganic Materials, Ibaraki, Japan 1994; Rietan-97Beta version 1997.

53. B. J. Wuensch, private communication.

54. M. J. Buerger, Proceedings of the National Academy of Science, USA **42**, 776 (1954).

55. E. Prince, NIST Rietveld Code.

56. J. Stalick, Workshop on Structure Refinement for Powder Data, National Bureau of Standards, Gaithersburg, Maryland, April 2-4, 1984.

57. A.C. Larson, R.B. Von Dreele, GSAS General Structure Analysis System, Los Alamos Neutron Scattering Center, Los Alamos National Laboratory, Los Alamos, NM (1985, 1994).

58. R. B. Von Dreele, "Combined X-ray and Neutron Rietveld Refinement," in *The Rietveld Method*, edited by R. A. Young, International Union of Crystallography, Oxford University Press, Oxford, 1-37 (1993).

59. M. Abramowitz and I.A. Stegun, "Handbook of Mathematical Functions," in Applied Mathematics Series 55, National Bureau of Standards, 771-802 (1966).

60. P. Thompson, D. E. Cox, and J. B. Hastings, "Rietveld Refinement of Debye-Scherrer Synchrotron X-ray Data from Al_2O_3," Journal of Applied Crystallography, **20**, 79-83 (1987).

61. G.Caglioti, A. Paoletti, and F. P. Ricci, "Choice of collimaters for a Crystal Spectrometer for Neutron Diffraction," Nuclear Instrument Methods **3** 223-228 (1958).